Improving the homogeneity of superparamagnetic nanoparticles and a study of their physicochemical properties

by

Barry Jay Yeh

A thesis submitted to the Graduate Faculty of
Auburn University
in partial fulfillment of the
requirements for the Degree of
Master of Science

Auburn, Alabama
August 6, 2016

Keywords: Iron Oxide Nanoparticles, Size-Selective Fractionation, Magnetic Resonance Imaging

Approved by

Allan E. David, Chair, John W. Brown Assistant Professor, Chemical Engineering
Mario R. Eden, Joe T. & Billie Carole McMillan Professor and Department Chair, Chemical Engineering
Thomas Hanley, Professor, Chemical Engineering

Abstract

Superparamagnetic iron oxide nanoparticles (SPIONs) have enormous potential in biomedical applications, including drug delivery, hyperthermia, and magnetic resonance imaging. However, the broad size distribution of SPIONs hinders translation from research results to clinical trials due to safety concerns and performance variabilities. Conventional size selection techniques fail to provide monodisperse SPIONs in comparison with other nanomaterials such as gold, silica, and other nanoparticles. Therefore, a new size fractionation method, diffusive magnetic fractionation (DMF), was introduced to solve current issues. The DMF separated different sized SPIONs by utilizing their mobility differences, which repeatedly released and attracted SPIONSs via a periodic magnetic field. The DMF performances showed independency from 5 different scaling conditions and less than 5% lost during the separation. The DMF separated SPIONs (DMF-SPIONs) showed much narrower in size distribution than conventional methods. In summary, the DMF was proved to be an efficient, scalable and controllable high performance separation method.

Table of Contents

List of Figures

Chapter 1: Introduction

People were fascinated by nanotechnologies over the past two decades, such as medicine, electronics, and solar cell applications. Applications of nanoparticles can be traced back to the first stained glass made for church windows in the mid-1100s, or the first green glass artifact made by ancient Egyptians. What enables the advancement of nanotechnology? It is the controllability achieved through modern science. The only measurement for nanomaterial a thousand years ago was visual determination. Therefore, major applications were for color effects. Modern analytical equipment, such as transmission electron microscope (TEM), scanning electron microscope (SEM), laser diffraction, or dynamic light scattering (DLS), can characterize color change due to differences in particle size and shape, as shown in **Figure 1**.

The effects of nanoparticles in the smallest biological entity, such as a cell, a virus, a gene or even a single string of protein, have been well studied. Among all nanoparticles, superparamagnetic iron oxide nanoparticles (SPIONs) attract the most attention in the fields of biomedicine and life science due to its unique combination of biocompatibility and magnetic property. SPIONs have been greatly used in preclinical studies, such as imaging contrast agents, tissue repair, magnetic hyperthermia, or drug delivery. The major challenge for SPION based applications is the lack of prominent examples in clinical applications, due to low reproducibility resulted from broad particle size distribution.

The effect of particle size distribution was historically overlooked. Nanoparticle's bio-distribution, cellular uptake, pharmacokinetics and imaging contrast are all strongly affected by particle size and size distribution [1,2]. In 2012, Dr. Sadrieh of US food and drug administration (FDA) emphasized the importance of particle size and size distribution for nanoparticle based platforms. It is even more important for SPION based platforms due to the

extreme difficulty in size distribution control, especially for particles larger than 20 nm. Therefore, we propose a scalable separation method to homogenize size distribution of SPIONs and enable the translation of the medical performance from preclinical stage to clinical applications and eventually to mass production of SPIONs for biomedical usages.

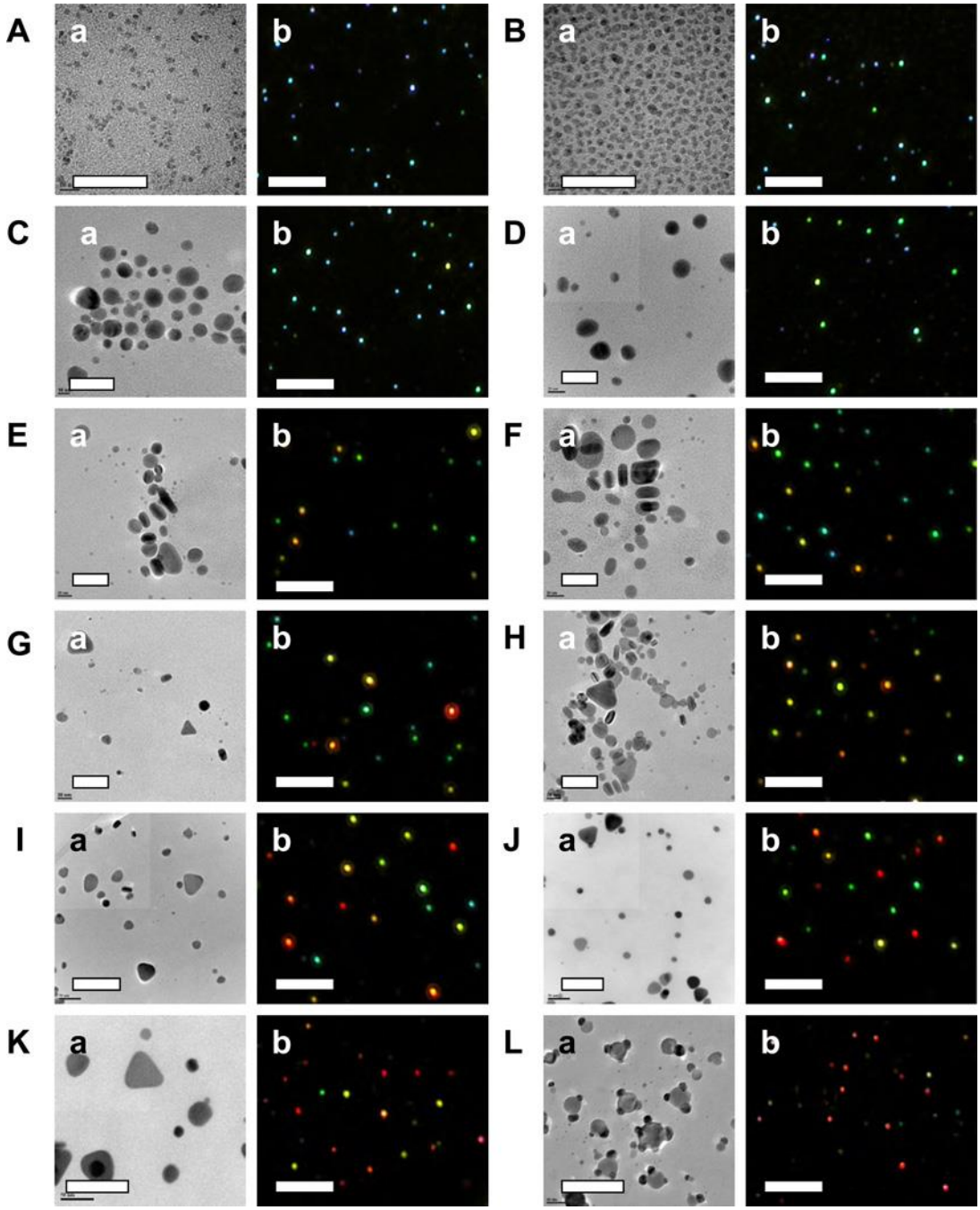

Figure 1. TEM (a) and dark-field optical microcopy and spectroscopy (b) of rainbow colored colloidal silver nanoparticles with different particle sizes and shapes [3].

1.1: Background

1.1.1: Superparamagnetism

Paramagnetic property is a physical state that materials are extremely easily magnetized and has zero magnetic moment without an external magnetic field, as shown in **Figure 2** and **Figure 3** [4,5]. Ferrimagnetic and ferromagnetic materials can be transferred to a paramagnetic state above its Curie temperature. For nanoparticles, the paramagnetic state can be achieved below the Curie temperature, this is called the superparamagnetic state.

Superparamagnetic characteristic can be achieved when thermal fluctuations are stronger than the magnetic interactions between particles, which is usually only achievable for nanomaterials or thin film structures [6]. Threshold sizes for single domain particles are usually larger than critical sizes for superparamagnetic characteristic [7]. Therefore, superparamagnetic nanoparticles usually contain single magnetic domains on each particle. For SPIONs, the critical size for superparamagnetism is about 30 ± 5 nm at room temperature; therefore, a critical size of 20 nm is usually used in most synthesis studies [7–11]. With an external magnetic field, SPIONs are magnetized to match the direction of the field by simply changing the particle orientation. In absence of an external magnetic field, random thermal fluctuation dominates the particle-particle magnetic interactions and results in zero overall magnetic moment of a population of particles [6]. The random thermal fluctuation avoids SPION aggregation and maintains particle colloidal stability due to magnetic repulsions and increases circulation life times in biomedical applications. On the other hand, ferromagnetic nanoparticles form large inter-particle structures and result in rapid clearance from biological systems [10,12,13]. Therefore, it is crucial to utilize the advantage based on the superparamagnetic characteristics of magnetic nanoparticles in biomedical applications.

1.1.2: Biocompatibility of SPIONs

The unique characteristic of superparamagnetic nanoparticles gives an opportunity for biomedical usages. Among all magnetic nanoparticles, iron oxide nanoparticle is one of the most commonly used material because of its biocompatibility and low toxicity [10]. The human body naturally contains 3500 mg of iron element at any time and about 50% is located within hemoglobin for oxygen transfer in blood [14]. SPIONs can be biodegraded into a part of the normal iron pool, such as ferritin and hemoglobin. Multiple SPION formulations are approved for clinical used around the world for different biomedical applications, such as Ferumoxytol (Feraheme®), Nanotherm®, Ferumoxides (Feridex®), Ferucarbotran (Resovist®), Ferumoxtran-10 (Combidex), and Feruglose (Clariscan®). Ferumoxytol was used for treatment of iron deficiency anemia and MRI contrast enhancement[15]. Nanotherm® was used for magnetic hyperthermia treatments in Europe [16,17]. The last four formulations are all MRI contrast agents which target liver, spleen and lymph system [18,19]. The enormous achievements are based on the foundation of strong biocompatibility and low toxicity of SPIONs in comparison to other commonly used nanoparticles, like gold and silica. Gold nanoparticles are not clinically approved and silica nanoparticles only have one formulation that has entered the phase I of clinical study [15].

1.1.3: The long lasting problem of SPIONs size distribution

SPIONs have enormous potential in biomedical applications that include: drug delivery, magnetic hyperthermia treatment, and magnetic resonance imaging [20–22,17]. However, a lot of biomedical studies still prefer to use silica and gold nanoparticles, because of the poorly controlled size distribution of SPIONs. The broad size distribution of SPIONs hinders translation of SPION performance to clinical use due to safety concerns and performance variabilities. The particle size distribution affects biodistribution and pharmacokinetics of

SPIONs and creates performance variabilities leading to safety concerns [1,23]. The size distribution affects the MRI relaxation time of SPIONs and results in inconsistent and unquantifiable MRI enhancement [24–27]. The size distribution also affects energy transformation, which causes magnetic hyperthermia treatment to rely on high SPION dosage or additional medical treatments [22,17,28]. For decades, the problem remains unsolved because of the limitations of chemical synthesis and failures of conventional size selection techniques in providing competitive monodispersed SPIONs in comparison with other nanomaterials such as gold, silica, and other nanoparticles [29,30].

1.1.4: Difficulties of evaluating the effects of SPION size distribution

Very few research studies focused on the effects of the size distribution of nanoparticles due to the difficulty in controlling and quantifying nanoparticle size distribution. There are several well-known techniques of quantifying particle size distribution; unfortunately, there is no comparison among the methods because the key measurement assumptions are based on quite different physical principles. For example, DLS measures the hydrodynamic size of a collection of nanoparticles. The result is quite different from most electron microscope measurements. Both TEM and SEM are electron microscopic techniques commonly used to determine particle sizes and size distributions. SEM images are based on the surface structure of nanoparticles which include the surface coating of most nanoparticles. On the other hand, TEM images usually are based on the core structure of nanoparticles. The particle sizes and size distributions are difficult to translate among different measurement methods. Therefore, it is very difficult to quantify the impact of particle size distribution only by literature reviews. The reason why particle size distribution is so important will be discussed in the following sections.

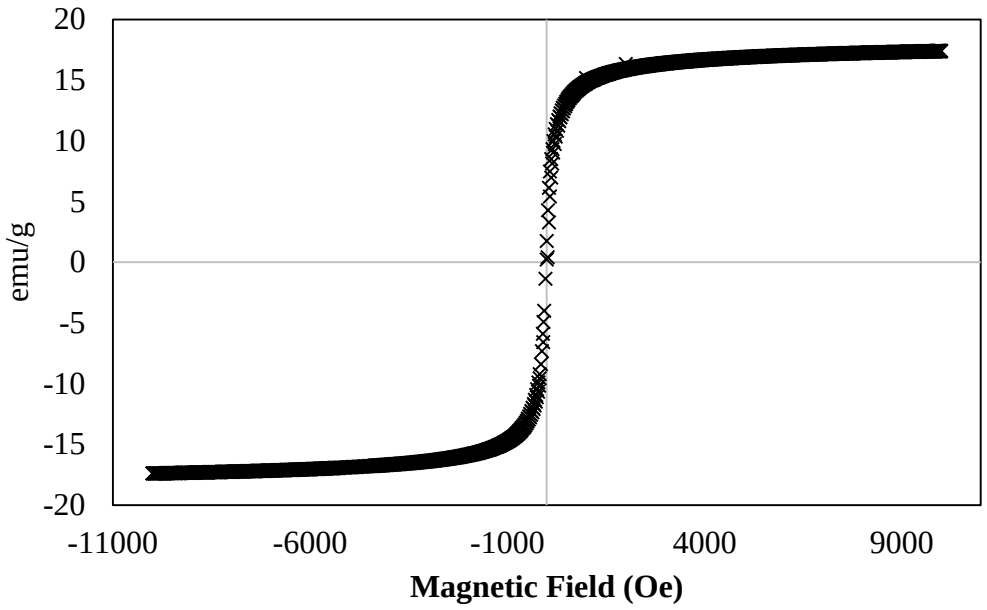

Figure 2. SQUID (superconducting quantum interference device) measurements of magnetic susceptibility of 50 nm starch coated SPIONs.

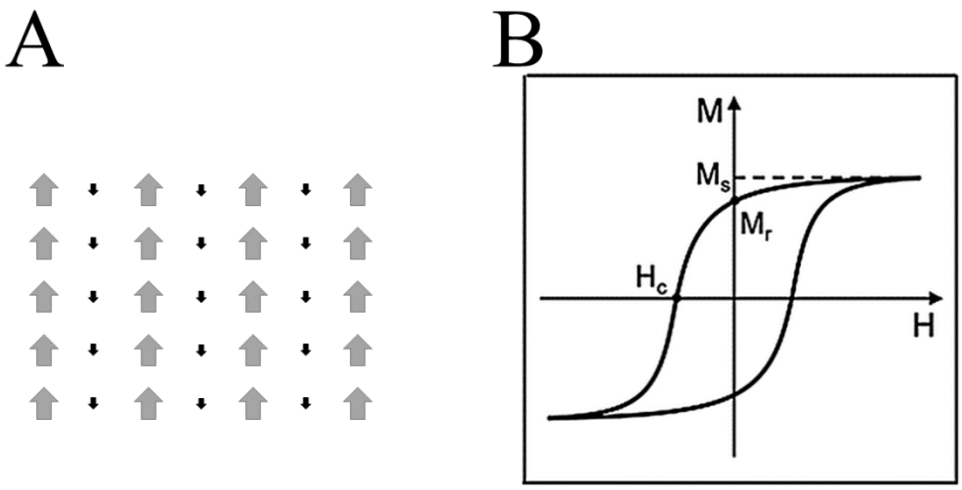

Figure 3. Ferromagentic material (A) the magnetic moments of multi-domain ferromagnetic material and (B) a typical hysteresis loop of a ferro- or ferromagnetic material where Ms, Hc and Mr are saturation magnetization, coercivity and remanent magnetization [4].

1.2: Particle size and size distribution effects on target delivery

In 1986, nanoparticles were observed to have enhanced permeation and retention (EPR) effect in tumor [31]. The US government has encouraged the development of nanoparticle based drug carriers since 2000 [32]. In the majority of applications, the biodistribution and the pharmacokinetics greatly determined the performance of nanoparticle carriers [33–35]. However, both the biodistribution and the pharmacokinetics were strongly influenced by particles sizes and size distributions. Different sized nanoparticles tended to accumulate in different areas of a biological system [1,23]. As a result, the particle size distribution will affect the amount of particle accumulation at a certain biological entity. Similarly, the pharmacokinetics of a nanoparticle have direct impact on the performance of the biomedical applications [34,36]. For most nanoparticle formulation, the size of the particles directly affects the pharmacokinetics [37–39]. In order to reach a targeted entity, nanoparticles have to overcome multiple biological barriers and avoid clearance from blood circulation, which makes the size of the particle important [37,40]. Recently, more studies focus on how the physical and chemical properties of nanoparticles affect their blood half-lives and bio-distribution. However, the effect of particle size distributions in a biological system remains unclear.

Researchers have been using different purification techniques to refine particle size distributions and to improve bio-distributions and performances of SPIONs. For example, SPION AMI25, Ferumoxide, has a broad distribution with an average size of about 150 nm, as shown in **Figure 4**. AMI25 was filtered to generate particles of 20 nm. Fractionated AMI25 was reported with a blood half-life of 15.9 h in rabbits in comparison to the original Ferumoxide of 0.46 h [20]. The difference in performances between different sized particles confirms the need for controlled size distribution for effective delivery in biomedical researches [37,41–44].

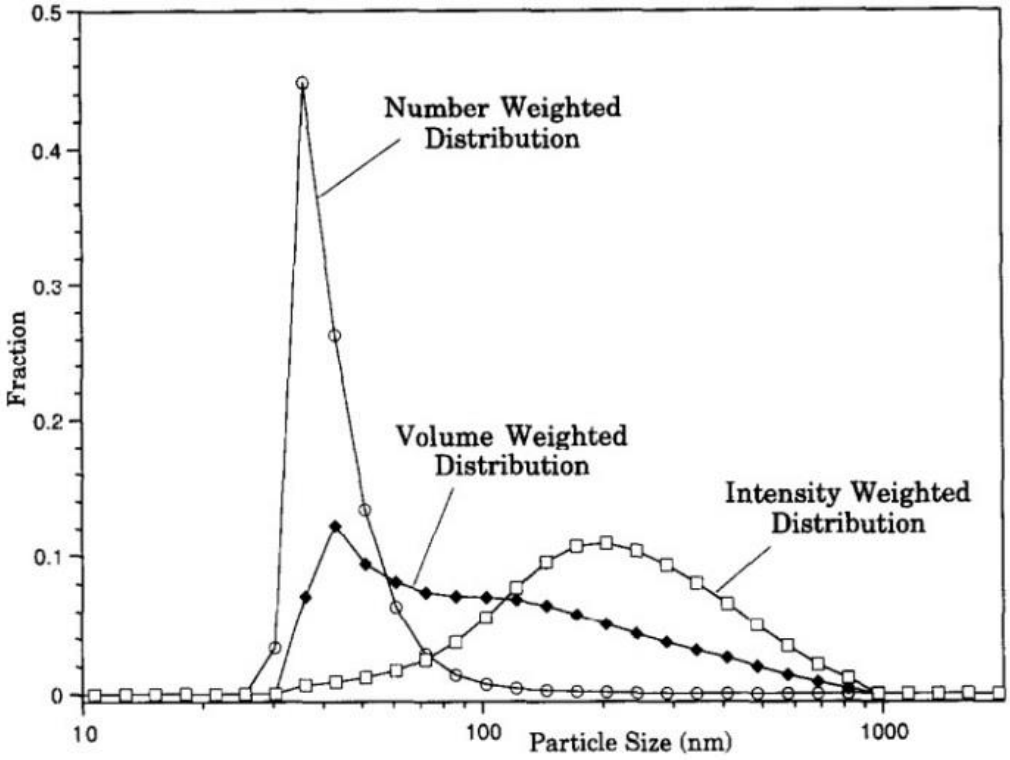

Figure 4. Ferumoxides lognormal particle size distribution by DLS (dynamic light scattering) [25]. The average sizes about 42 nm by number, 137 nm by volume and 250 nm by intensity. The particle size distributions are very board, which were estimated to be σ ~ 22% by number, σ ~ 89% by volume and σ ~ 62% by intensity. (σ = standard deviation/mean)

1.3: Particle size and size distribution effects on MRI application

MRI is obtained by applying perpendicular radiofrequency pulses to a constant magnetic field to induce magnetization and relaxation of protons within tissues. The T2 relaxation time is measured when protons emit the absorbed radiofrequency energy. The presence of SPIONs shortens the T2 relaxation time, which enhances the contrast of MRI. This phenomenon results from the magnetic field distortion near magnetic particles. The concept of MRI is based on the absorption and emission of radiofrequency energy from protons. The presence of SPIONs creates a magnetic field distortion interaction where the strong superparamagnetic character rapidly reacts to the oscillating radio frequency and accelerates the rate of energy release from the nearby protons. The field distortion significantly shortens the T2 relaxation time of protons and separates it from background noises, which makes SPIONs perfect candidates for MRI contrast agents.

Ferumoxides (Feridex®, Endorem®) and Ferucarbotran (Resovist ®, Cliavist®) are two types of SPIONs clinically approved as MRI contrast agents specifically for liver in the mid-1990s. Ferumoxides were developed by AMAG Pharma (former Advanced Magnetics) and were referred as AMI-25. The transverse (r_2) and longitudinal (r_1) relaxivites are 98.3 and 23.9 $mM^{-1}sec^{-1}$. Ferumoxides are 80-150 nm SPIONs with low molecular weight dextran coating. Ferucarbotran was developed by Schering AG, and was referred as SHU 555A [21]. Resovist is a carboxydextrane-coated SPION with 4.2 nm cores and a hydrodynamic diameter of 45-60nm. Its r_2 and r_1 relaxivites are 151 and 25.4 $mM^{-1}sec^{-1}$. The production of Ferumoxides was terminated in 2009 due to its inconsistent performances comparing to macromolecular gadolinium based contrast agents. Both SPIONs have very broad size distributions with $\sigma \geq$ 80%, as shown in **Figure 4** [25]. The broad size distribution results in an inconsistent enhancement on MRI because the relaxation time is strongly dependent on the particle sizes, as shown in **Figure 5** [24–27].

The broad size distribution of SPIONs also results in undesired offsite accumulation and low target accumulation. This results in high background noise signal with undesired side effects, such as back pains and headaches, reported by Bayer HealthCare Pharmaceuticals Inc. These effects are minimal for macromolecular based gadolinium contrast agents. However, Gadolinium based MRI contrast agents have toxicity concern due to leach of gadolinium ion from the complex [45,46]. In fact, researchers start to focus on Gadolinium oxide based nanoparticle as MRI contrast agent recently for a safer alternative, but offsite accumulations will become one of its major concerns [47]. In comparison, the low toxicity SPIONs become extremely attractive as a clinical substitution, particularly for patients with kidney diseases [46]. Both magnetic nanoparticles have to rely on a controlled particle size distribution to avoid the particle size variability. Monodispersed SPIONs will increase the accumulation of SPIONs in the targeted area, which further improves the MRI contrast. Therefore, monodispersed particles are the foundation for applicable, safer and higher contrast MRI agents for both iron oxide and Gadolinium based agents. This means the broad size distribution of current particles must be resolved.

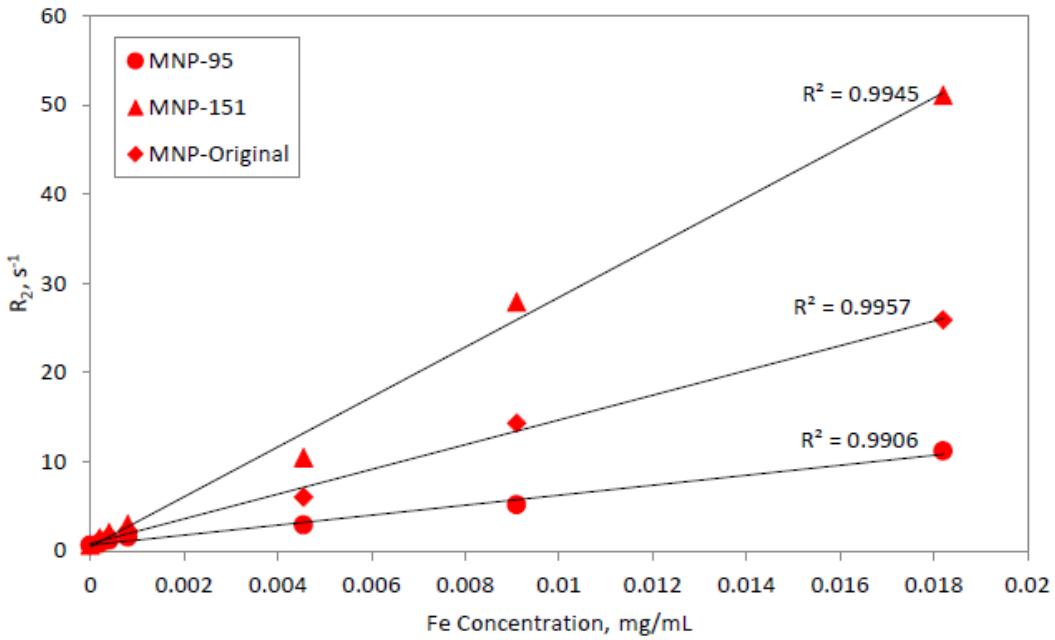

Figure 5. T2 relaxation time of different sized particles with different concentrations, which particle size average are 95, 151, and 100 respectively for MNP-95, MNP-151 and MNP-Original SPIONs [24].

1.4: Particle size effects on hyperthermia treatment

Magnetic hyperthermia treatment (MHT) is one type of medical therapy to weaken and destroy cancer cells by using a high temperature environment. The process involves magnetic nanoparticles to induce thermal energy. Magnetic nanoparticles will spin or oscillate in response to an external alternating magnetic field and thus generating a localized heating effect. However, heat localization is the a major challenge for MHTs because it determines treatment localization and therefore efficiency [48–50].

Most MHTs use multi-core SPIONs by the reason of their significantly higher heat transformation in comparison with single-core SPIONs [28]. Yet, multi-core SPIONs have a broad size distribution of $\sigma \geq 20$ %, where σ is the standard deviation of particle size distribution divided by the average particle size to represent particle size distributions independently from their particle average sizes [28,51,52]. The broad size distribution of SPIONs strongly affects their biodistribution and therefore reduces their treatment efficiency and localization [53,54]. Therefore, the MHT treatment is usually initiated with a direct injection of SPIONs into the tumor. Recently MHT showed successful results with Magforce (Nanotherm®) in the first clinical trials on prostate cancer, and approved by the European Medicine Agency [22,17].

The MHT with Magforce® involved direct injection of 4-12 ml of 112 mg Fe/ml of 100 nm aminosilane SPIONs with 15 nm cores into the tumor area [55]. Usually, MHT requires various additional treatments to improve the treatment performance, such as laser, microwave, radiation or other anticancer treatments, but most of them lead to harmful or fatal side effects [56–58]. Therefore, the treatment requires real time temperature control to ensure efficient treatment and avoid undesired effects [22,16]. After the clinical trial, it was stated that homogenous distribution of nanoparticles was the key for future MHT improvements as shown in **Figure 6** [22,16].

The heating efficiency must be improved for a safer and more material efficient MHT by reducing the need of high dosage injection to the target tumor. SPIONs with narrower size distribution provides a more efficient heat generation than SPIONs with a broader size distribution [59–63]. However, the production of monodisperse SPIONs is unachievable by the current technology. On the other hand, **Figure 6** showed inhomogeneous SPION distribution with very few particles traveled into the tumor region and resulted in a poor heat transformation. The SPIONs penetration through a physical barrier can be improved by low frequency alternation magnetic fields [64,65]. The effect can be further improved by monodisperse SPIONs as shown in **Figure 7**. In additional, chances of SPIONs internalization are also increased once SPIONs are near the cancer cell surface, which will result in significant decrease of the cancer cell survival rate by 40%, as shown in **Figure 8** and **Figure 9** [62]. Therefore, highly size controlled multi-core SPIONs is the foundation for future MHT improvements.

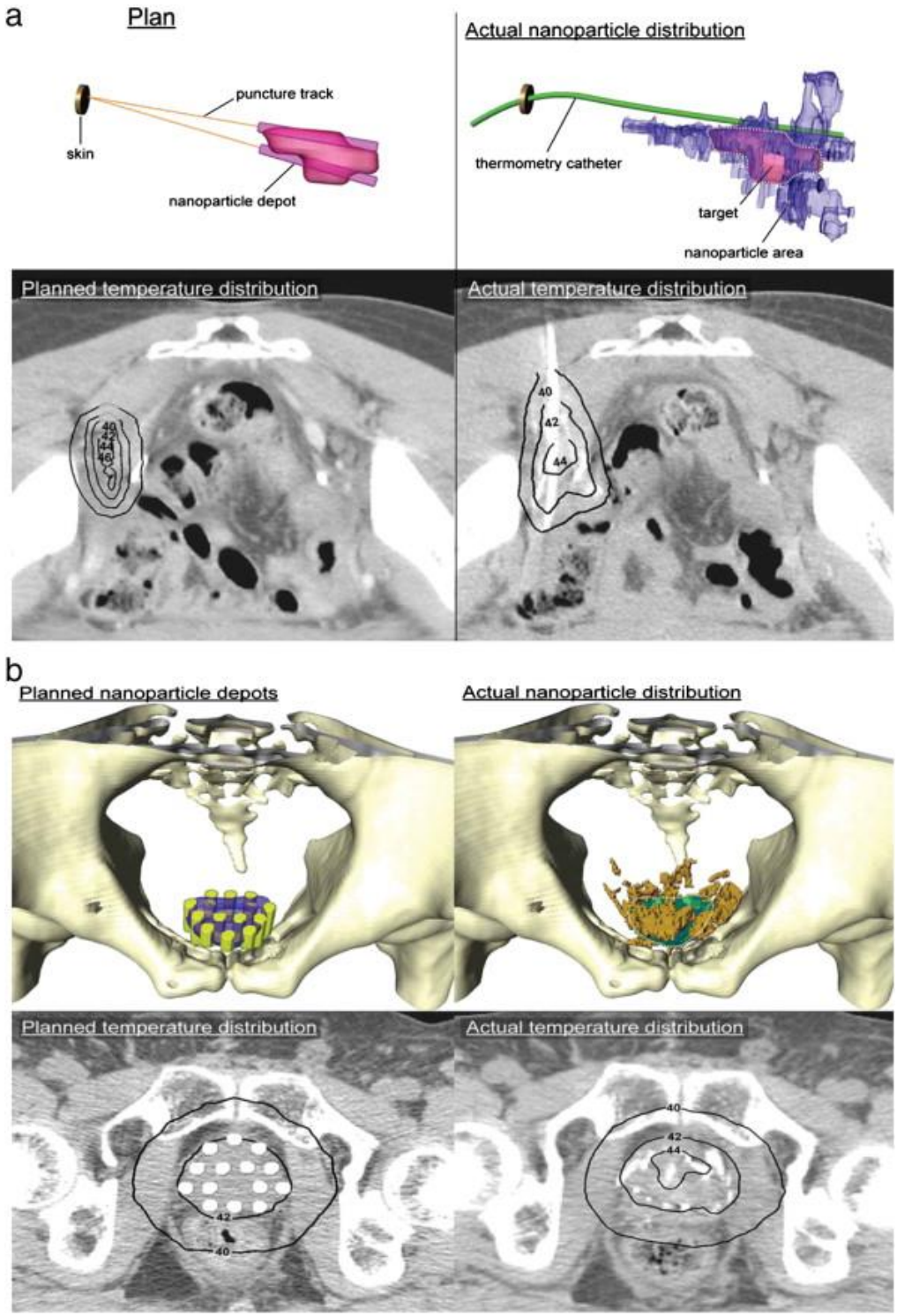

Figure 6. Comparison of the designed direct injections with real time temperature and particle distribution monitor system (a) cervical cancer of the pelvic wall and (b) prostate carcinoma[66].

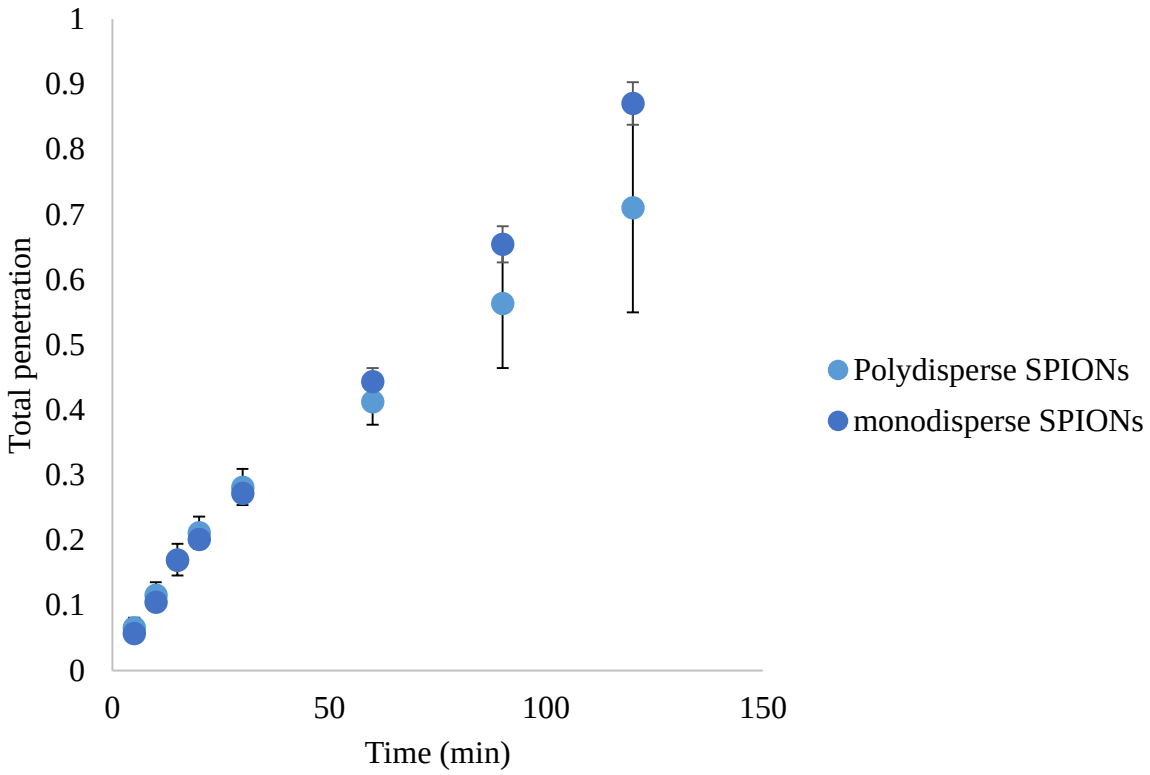

Figure 7. SPIONs with different size distributions penetrated through a 1μm membrane with a 7 Hz alternating magnetic field.

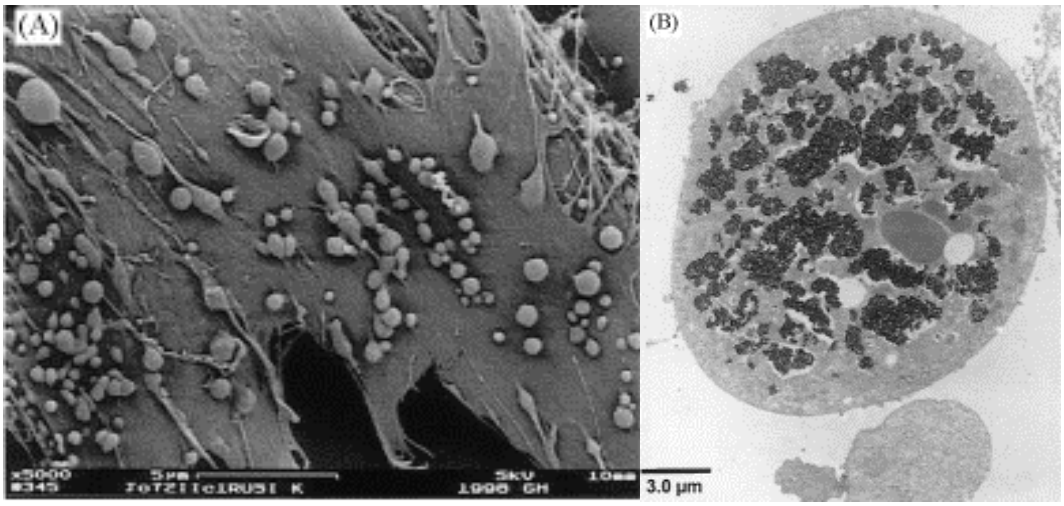

Figure 8, (A) Scanning electron microscopic (SEM) of SPIONNs on cell surface. (B) Transmission electron microscopic (TEM) of SPIONs aggregation on cell surface [62].

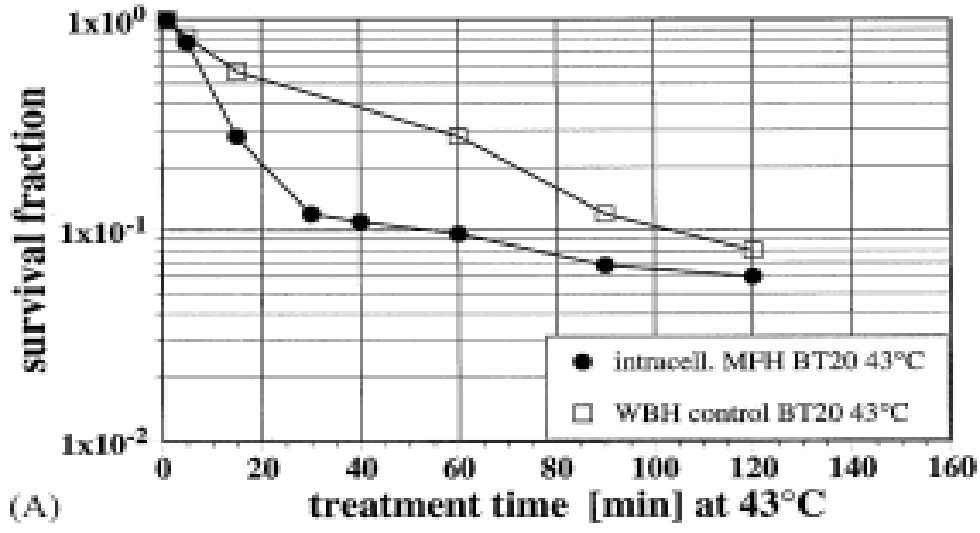

Figure 9, intracellular hyperthermia cell survival rate (black dots) and extracellular heating survival rate (white dots) [62].

1.5: Single- and multi- core SPIONs

Magnetic materials have unpaired electrons, lone electrons with half-entry electron configurations, which generate magnetic moments. Non-magnetic materials usually have electrons in pairs, a positive magnetic moment and a negative magnetic moment, which result in a total magnetic moment of zero. SPIONs are usually synthesized with shell and core structure, and the core material is usually magnetite. Magnetite (Fe_3O_4) has the strongest paramagnetic property of all natural occurring minerals and shows superparamagnetic characteristics below its critical size of 30 nm [8,67]. Therefore, SPIONs smaller than 20 nm are usually synthesized with single core and shell structure, and they are also called ultra-small SPIONs (USPIONs). Particles larger than 20 nm are usually made with a multi-core structure that contains multiple USPIONs held together by an external matrix.

The shell of SPIONs can be made with different materials to improve the performance and compatibility for different applications. For example, PEGylation, a poly(ethylene glycol) coating can improve the biocompatibility of iron oxide nanoparticle [68–70]. Dextran and Polyvinylpyrrolidone (PVP) coatings enhance the blood circulation time [11]. Polyvinyl alcohol (PVA) coating prevents aggregation and narrows the size distribution.

The core of the SPIONs determines the magnetic properties of the particle. Most synthesis process can produce both USPIONs and multi-core SPIONs with different reaction conditions. USPIONs have better synthesis controls in particle sizes, size distributions, compositions and particle shapes [71–75]. USPIONs also have a higher cell uptake, longer blood circulation and higher penetration of capillary wall than multi-core particles [41]. USPIONs nanoparticles usually have a particle size distribution of $\sigma \leq 5\%$ [76]. The distribution of USPIONs are mainly controlled by reaction time, pH, iron content, and polysaccharide content [77]. On the other hand, multi-core particles are poorly controlled in size, size distribution, and composition [28,51,77,78]. Multi-core SPIONs have very different advantages from USPIONs, such as large surface area, higher energy transformations and higher MRI contrast [28]. Except

Feruglose, all the current clinically approved SPIONs are multi-core SPIONs [15,18,19]. The synthesis of multi-core particles has less control over the particle properties in comparison to USPIONs, as shown in **Figure 10**. The size distribution of multi-core SPIONs is usually very broad with $\sigma \geq 20\%$ [28,51,52]. Therefore, additional size fractionation techniques are necessary for multi-core SPIONs to be used in biomedical applications. However, conventional size selection methods are not able to produce multi-core SPIONs with narrow distribution comparable to USPIONs, which will be discussed in section 1.8.

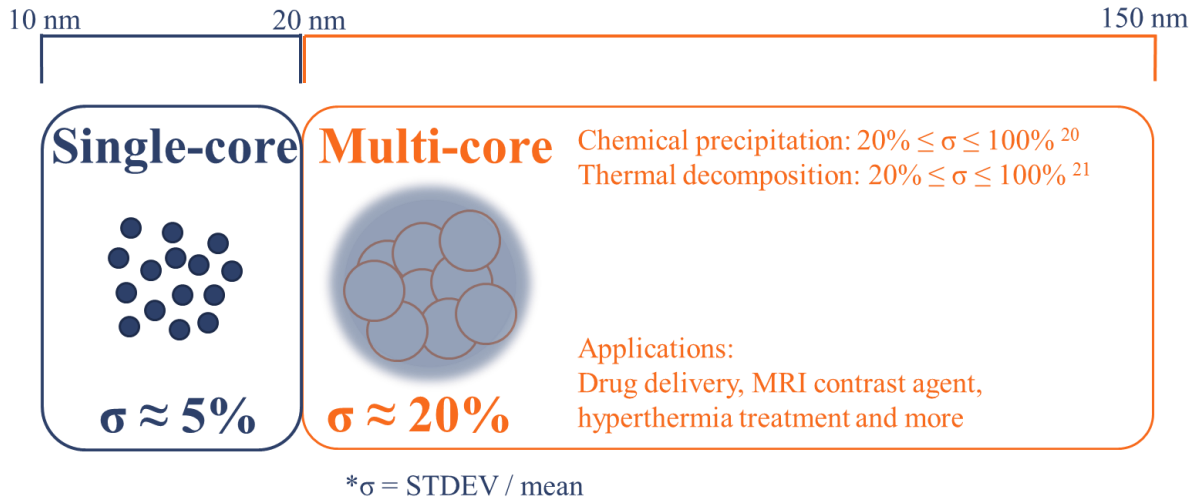

Figure 10, structure, average size (scale on top) and size distribution σ comparison between single- and multi-core synthesized SPIONs. Multi-core SPIONs can be made smaller than 20nm, but single-core SPIONs cannot be larger than 20 nm when synthesize in room temperature.

1.6: SPIONs synthesis

As mentioned in the previous section, multi-core SPIONs are multiple USPIONs held together by an external matrix, which is usually a chemical or polymer coating. Physical synthesis such as gas phase deposition and electron beam lithography are rarely used due to the difficulty in controlling nanoparticle sizes [79–82]. On the other hand, chemical synthesis methods have better controls on particle properties and scalability. Most chemical synthesis methods and coating techniques for USPIONs can be further reacted to generate multi-core SPIONs, such as thermal decomposition[73,76,78], chemical precipitation[83,84], and micro-emulsion[85]. However, the size distribution for the multi-core SPIONs is very broad with $\sigma \geq 20\%$ regardless of different synthesis methods [28,51,52]. The reason of the broad size distribution can be generalized by the complex structure of multicore SPIONs. The internal structure of multi-core SPIONs is actually associated with how the nucleus are assembled. Particle cores tend to aggregate immediately after their formation. These primary aggregation leads to the internal structure of multi-core SPIONs [28].

1.6.1: Chemical precipitation method

For chemical precipitation method, changing the initial ratio of reactants will result in different sizes and structures of multi-core SPIONs. The particles can then be stabilized with a polymer or molecular coating. Both Feridex® (Endorem®) and Resovist® (Cliavist®) are chemical precipitated multi-core SPIONs with polymer coatings, and approved by the FDA for MRI contrast agent specifically for liver. Feridex® are dextran coated and Resovist® are carboxydextran coated multi-core SPIONs with 4-8 nm cores in a very broadd overall size distribution [25].

Chemical precipitation method is the simplest method for iron oxide nanoparticle preparation. The iron oxide nanoparticle preparation starts with an overall chemical reaction as follows [83,84]:

$$Fe^{2+} + 2Fe^{3+} + 8OH^{-} \rightarrow Fe_3O_4 + 4H_2O. \quad (1)$$

Iron chloride ions reactant alkaline can provide iron oxide particles under oxygen-free atmosphere, which is achieved by nitrogen bubbling through the reactor. The oxygen-free condition not only protected the reactant from oxidation but also provided a better control of particle size [86,87]. In general, the ideal pH range is 9 to 14 with a molar ratio Fe^{2+} to Fe^{3+} of 2:1 for a complete precipitation [11]. Theoretically, Iron oxide particles form tiny crystalline nuclei and then is followed by crystal growth during the precipitation process [83]. The particle precipitation process is believed to follow two paths. One is a dynamic equilibrium, where particle precipitation proceeds by addition and removal of monomers, such as molecules and ions [11]. Therefore, the growth of a particle will consume the removal materials of other particles. This mechanism is called Ostwald ripening, and is assumed to be the main path of crystal growth [88]. Therefore, the particle size is controlled by the growth of crystalline, which can be controlled by temperature and reactant concentration. The second path is called oriented attachment, where anatase and iron oxide nanoparticles with a few nanometer are able to aggregate under hydrothermal condition [89–91]. The oriented attachment creates a dislocation on the crystal interface, and results in iron oxide nanoparticles with multiple crystal structures. The particle size grows with time, and the reaction can be terminated by decreasing temperature. The products usually contain a black color mixture of magnetite, maghemite, and diamagnetic components with magnetic saturations about 30-50 emu/g [92].

Different chemical synthesis methods by precipitation result in different SPIONs compositions and different magnetic properties [93]. The size distribution of USPIONs from chemical precipitation is usually $\sigma \geq 10\%$ [93]. Therefore, an additional size-selection process is needed to control core distribution. The most common size selection method for USIPONs is

to precipitate out the large particles by adding poor solvent. In polydispersed particle mixture, larger particle precipitates faster than smaller ones. These particles can be separated by centrifugation. Particles with unwanted size range can be re-dissolved and recycled. A particle size distribution of $\sigma \leq 5\%$ can be achieved through precipitation process. The particle shape is usually spherical. For multi-core SPIONs, other fractionation techniques need to be used to improve the size distribution, which will be discussed in the following sections. The internal structures of the multi-core SPIONs are decided by reaction conditions when the nucleus are formed. As mentioned in previous context, this initial nucleus aggregate and form the internal structure of multi-core SPIONs, including shapes and the numbers of particle cores [28].

1.6.2: Thermal decomposition method

One approach is to inject organometallic compounds into a high temperature surfactant solution and to generate nuclei instantaneously. The other one is a controlled heating process with organometallic compound already in a surfactant solution, particles grow at high temperature and the reaction can be terminated by controlling the temperature [73,76,78].

Thermal decomposed USPIONs were highly monodisperse $\sigma \leq 5\%$ with cubic or spherical shapes, and with no need of a secondary size selection process [73,76]. The process is usually done with iron pentacarbonyl and iron acetylacetonate in oleic or benzyl ether or iron oleate. Thermal decomposition requires a secondary process, e.g. ligand exchange, to stabilize particles in a biocompatible aqueous phase to exchange for the surface-coating oleic acid molecules by DMSA (dimercaptosuccinic) molecules. This process involves the oleic acid coating particle in toluene mixed with DMSA in DMSO (dimethylsulfoxide) for several hours until the ligands exchange. Following the ligands exchange process, the particle needs to be washed several times to remove toxic materials. However, multi-core SPIONs still have a broad distribution and require additional size selection method to narrow the size distribution [73,76,78].

1.6.3: Micro-emulsion method

Micro-emulsion is formed with two immiscible liquids with interphase films of surfactant to stabilize its structure [85]. For a water-in-oil emulsion, the aqueous phase forms 1-50 nm droplets. These aqueous droplets are surrounded by oil containing soluble metal salts. These droplets will continuously merge with other droplets or collapse to form new droplets. As a result, particle nuclease is formed once precipitation occurs. The nuclease will aggregate when the aqueous droplet merge with another, and finally the particle will be extracted from the droplets [94–96]. The process is difficult to be scaled up and to produce monodisperse multi-core SPIONs.

1.7: Dynamic Light Scattering (DLS) size measurement

DLS is a method to measure particle size by observing light scattering fluctuations from particles with Brownian motions. The movement of a particle results in an intensity change of the scattered light. As a result, scatter light fluctuates with multiple particles. The frequency of the scattering fluctuations depends on particle sizes. For example, smaller particles have rapid Brownian motions and can generate high frequency fluctuations. The frequency of the fluctuation can be correlated to the overall particle velocity in terms of translational diffusivity. The diffusivity can then be used to determine the particle size by the Stoke-Einstein equation.

$$D_h = \frac{k_B T}{3\pi\eta D_t}$$

The concept was first mentioned in Einstein's PhD thesis to calculate the Avogadro's number, where D_h is the hydrodynamic diameter, k_B is the Boltzmann constant, T is the temperature, η is the dynamic viscosity, the D_t is the translational diffusion constant and D_h is the hydrodynamic diameter. k_B, T, η are known constants and D_t is determined by a correlation function. There are three common approaches to determine the translational diffusion constant, D_t, which are Cumulants, fitting to a known distribution function, and inversion of Laplace transform [97].

For this research, intensive study is based on the DLS measurements for both particle sizes and size distribution. Two of the most important DLS measurement are the Z-average size and the Polydispersity index (PdI). Both parameters are determined from the cumulant fit, which is an approach to fit the correlation function. The Z-average is also known as the cumulant mean obtained from the first parameter of the cumulant fit to the correlation function, which gives the average particle size by the intensity of the scattered light. On the other hand, PdI is the second fitting parameter of the cumulant fit, which is used to estimate the randomness of the data. Therefore, it is also used to represent the distribution of the samples in many

researches. Both parameters are measured by standard procedure ISO 13321 and ISO 22412 by Malvern Zetasizer ZS.

1.8: Review of magnetic nanoparticle size selection methods

As mentioned in the previous sections, SPIONs with diameters greater than about 20 nm are generally synthesized with multi-core structures held together by an external matrix. This typically yields particles with a very broad size distribution with DLS PdI of above 0.3 [98]. This broad size distribution hinders clinical translation of these particles due to safety concerns and performance variabilities. In fact, there were multiple attempts to narrow SPION size distribution in the past two decades, but none of them were really controllable and scalable, including vacuum filtration, gel chromatography, centrifugation separation, and magnetic fraction technique (MF).

Quantifying size distribution is not an obvious job by comparing data between different measurement methods. Currently, there are no optimal means to measure size distribution of nanoparticles for different applications. In general, monodisperse nanoparticles are particles that has a $\sigma \leq 5\%$ standard deviation by its mean size, or a PdI value lower than 0.1 [83,99–101]. None of the currently used SPIONs have reported a monodisperse size distribution within the range even in a small quantity for research purpose.

Gel chromatography and vacuum filtration techniques have their limitations in scaling-up and generating multiple fractionation from a polydisperse distribution [20,37]. Both processes utilize particle mobility differences to separate different sized particles through material matrixes by a filter or gel. Particles were hard to be recovered from the matrix to produce multiple fractionations. Moreover, the separations were limited by the homogeneity of the pore size and the structure of matrix material, which maybe the reason for the large size distribution, as shown in **Table 1**.

Centrifugation was able to generate multiple particle separations by applying different rotational speeds [102]. The process utilizes centrifugal forces to separate different sized particles into two layers which consist of suspended particles and aggregated particles. It is difficult to

have a complete removal with only the suspended particles without the aggregated particles, which may also cause large size distribution as shown in **Table 1**.

The MF technique has its potential for large quantity of production, but it has the worst size distribution controllability among all three methods, shown as in **Table 1**. The concepts and methods will be discussed in the following sections.

Separation method	Average size (nm)		Core	Size measurement method	Size distribution		Coating molecule	Application/notes	Ref.
	Ori.	Sep.	(nm)		Ori.	Sep.			
Gel Chromatography	72 (DLS)	11.4	4-7	TEM	NA	± 6.3 nm	Dextran	MRI contrast agent	[41]
MF	34.4	7.7 14.4 28.8 37.7 44.4 47.7 68.8	3	DLS (z)	PdI ~ 0.35	PdI ~ 0.27	Carboxydextran	Size separation	[98,103]
Vacuum Filtration	121 (Feridex)	15.1	NA	DLS (z)	broad	PdI = 0.2	Dextran	MRI contrast agent	[20]
Centrifugation	NA	65.5 38.9 23.1 18.5	NA	DLS (v)	broad	± 14 9.1 6 4.4 nm	SiO2	MRI relexivity comparasion	[102,104]
	~6 (n), ~19 (v)	14.9 13.2 12.1 7.3		XRD		NA			
	~13 (n), ~20 (v)	24.2 20.0 15.8 10.5		TEM		± 2.4-3.6 nm			

Ori.: original samples before any size separations

Sep.: size separated samples

(n): number weighted measurement

(v): volume weighted measurement

(z): z-average size

NA: not available

broad: $\sigma \geq 80\%$

Table 1. Comparisons between current separation methods for SPIONs.

1.9: The MF technique

The MF technique was suggested by Thomas Theinländer et al in 2000 [98]. The method was designed as an approach to study particle size effect on different size SPIONs, including blood half-lives, and MRI relaxivity [41,105,106]. The separation started with a strong magnetic force and captured all SPIONs. Once all the SPIONs were captured by the magnetic field, a fluid flow was introduced to the SPIONs. Smaller size SPIONs were released from the field due to weaker magnetic attraction. The magnetic field strength then decreased stepwise and generated multiple fractionations with different sized particles.

However, multiple populations were usually observed with MF-SPIONs (magnetic fractionated SPIONs) and resulted in a broad size distribution with high PdI values, as shown in **Figure 11**. The multiple populations remain the same before and after sonication or additional MF processes. The hypothesis was that larger SPIONs were blocked by smaller SPIONs from reaching the magnetic source and therefore had a weak magnetic attraction. Smaller SPIONs that were close to the surface of the magnetic source aggregated on the surface faster than larger SPIONs because of their shorter distance, and blocked the late comer larger SPIONs to reach the surface of the magnetic source even with larger magnetic contents, as shown in **Figure 12**. The larger SPIONs were forced to be immobilized away from the magnetic source because of a weaker magnetic attraction, and therefore they were released with the smaller SPIONs when the magnetic field decreases and vice versa. In fact, SPIONs were clearly separated by their average size in the system, but their PdI only decreased slightly from about 0.35 to about 0.27 [98]. The size distribution was not improved significantly and the fractionated particle was still polydispered in multiple studies [106,107].

The effects of the broad size distribution of MF-SPIONs was observed in different follow up researches. The blood half-lives of MF-SPIONs can be extracted from a study done by Thomas Allkemper et al, 2002 [106]. The study reported a MRI contrast drop over time by different size MF particles in rabbits with MF-SPIONs separated from SHU-555 SPIONs. The

changes of MRI relaxation time were due to the changes in average size of different MF-SPIONs. Unfortunately, even the smallest MF-SPIONs with an average size of 21 nm had blood half-lives in enhancement performance only around 15~25 minutes. This result is a huge difference comparing to studies done by vacuum filtration and gel chromotagraphy methods, which showed strong size dependency of blood half-lives. Karen C. Briley-Saebo al et reported a huge blood half-live increment from 0.46 h to 15.9 h in rabbits after Ferumoxides was fractionated by vacuum filtration into 20 nm [20]. Similar result was observed in rats, blood half-live had an increment from 6 min to 81 min by filtrating through gel chromatography [41,108].

The significant difference in results might come from broad size distribution of MF-SPIONs due to poor separation performance. Both gel chromotagraphy and vacuum filtration methods significantly provide narrower size distribution SPIONs comparing to the original broad size distribution, while MF did not, as show in **Table 1**. MF was used as a supplemental size selection treatment for different synthesis to produce different sized particles, but none of them reported a significant improvement in results [107,109,110]. Particle size distribution is a very important factor for blood half-lives and therefore a new size fractionation method is needed for biomedical applications.

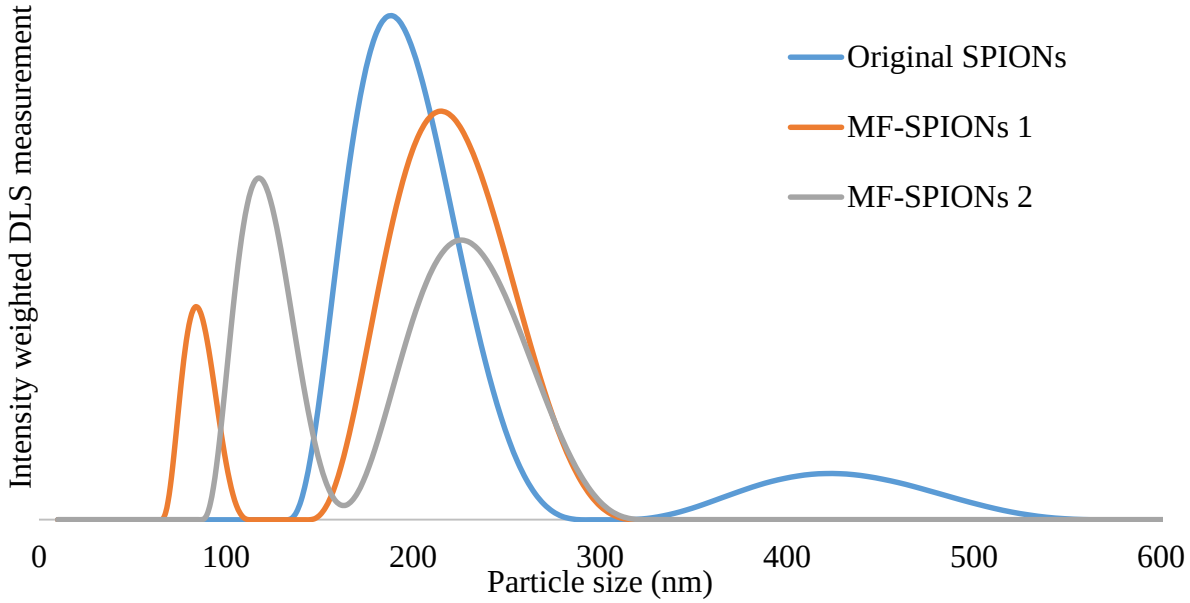

Figure 11. Intensity weighted DLS measurement of MF- SPIONs and their original SPIONs.

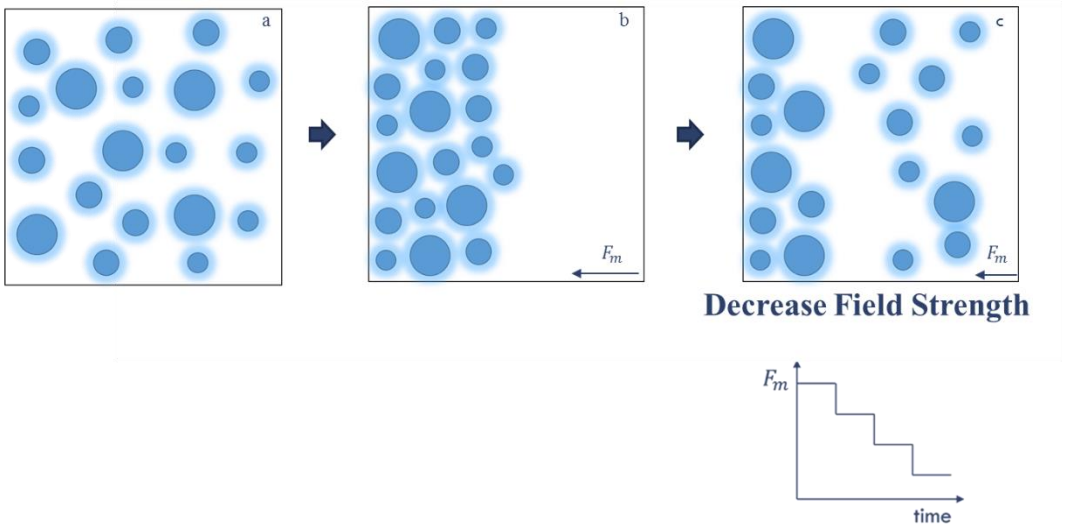

Figure 12. Illustration of MF mechanics of magnetic fractionation.

Chapter 2: The discovery of an effective size fractionation method for SPIONs

2.1.1: Introduction of diffusive magnetic fractionation

The goal of this project is to provide an efficient, scalable and controllable size fractionation process to provide monodisperse SPIONs. Therefore, a novel, efficient, controllable and scalable size fractionation method, called diffusive magnetic fractionation (DMF), for the production of monodisperse SPIONs was invented. DMF has much better performance than the conventional MF method which is the only scalable size fractionation method reported in literature. DMF is able to efficiently provide multiple fractionations of monodisperse SPIONs with a high particle recovery and different surface chemistries. DMF is designed to be scalable so that its performance is independent of process volume and its products can be predicted and controlled by mathematical models.

2.1.2: Concept of DMF

The DMF was designed by utilizing the difference in diffusivity and magnetic mobility of different sized particles by a periodic magnetic field (PMF). The PMF separates polydisperse SPIONs into multi-layered organized structures which contain monodisperse SPIONs in each layer. DMF immobilizes larger particles at the surface of the magnetic source due to its large magnetic content and slow diffusion rate. Therefore, only smaller SPIONs will be released from the system when the magnetic field decreases, as shown in **Figure 13**. Therefore, DMF can significantly narrow the size distribution down to the monodisperse range with PdI values ≤ 0.1.

The DMF process consists of two steps. Firstly, apply a PMF to create the multi-layered structures. Lager SPIONs move toward the magnetic source faster than smaller SPIONs due to their stronger magnetic attraction. Without the magnetic field, larger particles diffuse slower

than smaller particles due to their larger particle size. Therefore, the polydisperse SPIONs are attracted and released repeatedly under the PMF. Eventually, larger particles will be trapped in the inner layer of the structure due to slower diffusion rate and stronger magnetic attraction. On the other hand, smaller SPIONs will be forced to settle on the outer layer owing to weaker attraction and faster diffusion rate. Secondly, reduce the strength of magnetic field in order to release the smaller particles. The outer layer of smaller particles will leave the structure, due to strong diffusion and weak magnetic attraction, as shown in **Figure 13**. Multiple fractionations can then be generated by stepwise decreasing the magnetic field.

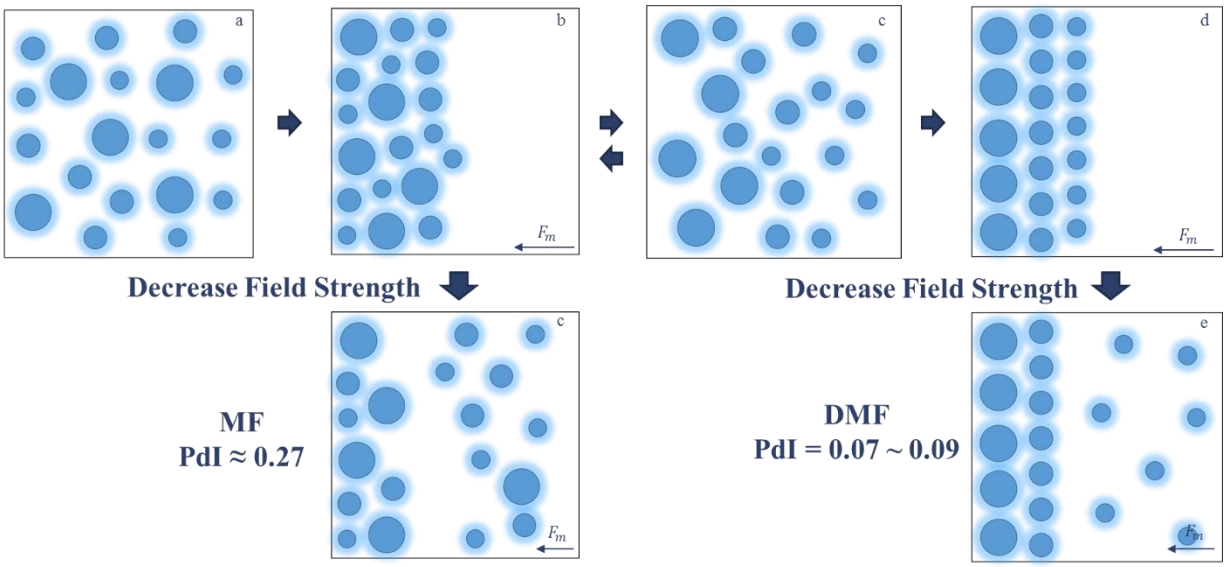

Figure 13, illustrates the difference between MF and DMF techniques. (a) SPIONs suspense inside a solution without any external magnetic field. (b) Polydisperse SPIONs immobilized by an external magnetic field. (c) SPIONs release from the magnetic field with a PdI ≈ 0.27, which is the MF technique. (d) Continuation from (c) with a PMF. Displacements were created between different sized SPIONs where larger SPIONs are closer to the magnetic source and smaller SPIONs are away from it. (e) SPIONs were immobilized by an external magnetic field and formed a multilayer structure. (f) SPIONs are release from the field by position which contain monodisperse smaller SPIONs with PdI = 0.07 ~ 0.09.

2.2: Experiments

2.2.2: Materials

FluidMAG-D (starch-coated magnetite (Fe3O4)) iron oxide nanoparticles (75mg/mL) were obtained from Chemicell® GmBH (Berlin, Germany). Succinimidyl polyethylene glycol (mPEG-NHS) of molecular weight 5 kDa was obtained from Nanocs (New York, NY). Dimethyl sulfoxide ((CH3)2SO, 99.9%) was obtained from BDH Chemicals. Epichlorohydrin (C3H5ClO, 99%) was obtained from Alfa Aesar. Sodium hydroxide (NaOH, 97%) was obtained from BDH chemicals. Ferrozine iron reagent, monohydrate was obtained from J.T. Baker. Neocuproine hydrochloride monohydrate (C14H12N2·HCl·H2O, 99%) was obtained from Acros. Ammonium acetate, and ACS (CH3COONH4, 97% min) was obtained from Alfa Aesar. L-ascorbic acid (C6H8O6) was obtained from BDH. Iron standard solution (1.00 mg/L as Fe) was obtained from HACH. Deionized water was obtained by using an ELGA PURELAB Flex water purification system.

2.2.2: Characterization of SPIONs

ZetaSizer Nano ZS90 (Malvern, Worcestshire, UK) was used to measure particle hydrodynamic diameters, particle size distribution and Zeta potentials. Both DLS and Zeta potential measurements were taken in triplicate by the sizing instrument.

Superconduc1ing Quantum Interference Device (Quantum Design, US) was used to measure the magnetic susceptibility of SPIONs.

SpectraMax i3 (Molecular Device, US) was used to measure optical absorbance of samples.

Ferrozine Assay was used to measure the iron content of SPIONs. Iron standards were made by mixing 33.24 uL of stock iron solution at 1000 mg/L with 1123.5 µL 10 mM HCl and

diluted into 0.25, 0.2, 0.15, 0.1, 0.05, 0.02, 0.0075, and 0 nmol/µl. The standards were prepared in triplets and then put into a 24 well plate. SPION samples were made with 1:4000, 1:2000, 1:1000 dilutions for starch coated SPIONs, aminated SPIONs and PEGylated SPIONs respectively. SPION samples were also prepared in triplets and placed in another 24 well plate. Then, 200 µl of iron releasing reagent was added into all the wells which were sealed with Aluminum foil for both the standards and the SPION samples. The iron releasing reagent was prepared by mixing equal volumes of 4.5% w/v $KMnO_4$ with 1.4 M HCl. Both 24 well plates were vortexed for 1 minute at 650 RPM. Both well plates were incubated for 2 hours at 60 °C and then cooled down for 10 minutes in room temperature. Then ferrozine was added into all the wells. The ferrozine was prepared by mixing 9.95 mg of ferrizine, 5.12 mg of neocuproine, 578 mg of ammonium acetate, 528 ascorbic acid and 3 ml of water. Both 24 well plates were incubated in room temperature for 30 minutes. Finally, 280 µl of each samples were transferred from 24 well plate to a 96 well plate and measured the absorbance at 550 nm.

2.2.3: Processes

SPION surface modification process was used to observe effects from different surface chemistries. The commercially purchased starch coated SPIONs were cross-linked, aminated, and PEGylated according to previously published method[112]. The method starts with 2 mL of starch coated SPIONs solution (22 mg/ml) incubated with 2.6 mL 6M NaOH for 15 minutes. Then, 1.3 mL of epichlorohydrin was then added and incubated for 24 hrs at room temperature. The resulting SPION solution was dialyzed against water with an 8-10 kDa MWCO Float-A-Lyzer® G2 dialysis device (Spectrum Laboratories, Inc., Rancho Dominguez, CA). The purified SPION solution was then incubated with 2 ml of 30% ammonia for 24 hrs at room temperature to provide aminated SPIONs. The PEGylated SPION was obtained from mPEG-NHS. Firstly, 15mg of 5 MW of mPEG-NHS was dissolved in a mixture of 300 µl DMSO, 300

µl water and 300 µl phosphate buffer. A 300 µl of aminated SPION solution was added into the mixture and was shook for 24 hrs at room temperature. The resulting mixture solution was then magnetically separated from solution and washed with DI-water for 4 times.

Magnetic column, an iron bead packed column LS Column Miltenyi Biotec, was used to increase system capacities. The column went through an 22W electric coil that was connected to a DC power supply (Hewlett Packard 6543A) to provide an external magnetic field, as shown in **Figure 14**. The magnetic field has a linear proportionality with the input current of the electrical coil, as shown in **Figure 15**. Therefore, the input current of the electrical coil was used to describe the magnitude of the magnetic field in this document.

MF process was used for comparison with DMF. a constant current of 300 mA was applied immediately after the column was fully loaded with the SPION solution. After 15 minutes, a continuous aqueous flow with 1.5 ml/ min was introduced to the system and the field strength was decreased stepwise to release a fractionation on each decrement. During each decrement the particles were collected either directly or from the flow output or a second magnetic column with a strong magnetic of 0.22 T. The fractionations were collected until the aqueous solution turned clear. Then the magnetic field was reduced again to release multiple fractionations.

DMF process was used to homogenize SPIONs by their size differences. After polydisperse SPIONs solution filled the magnetic column fully, the input current was turned on and off periodically to provide a PMF for multiple cycles. Different PMF cycles and period parameters were used for different sized and surface coated SPIONs. In general, a PMF with 2/5 (on/off minutes) and with 21 periodic cycles was used for starch coated SPIONs. After the PMF process was finished, an aqueous flow ran through the column continuously with a flow rate of 1.5 ml/min, and then the magnetic field was decreased stepwise to release a fractionation at each decrement. The fractionations were collected until the aqueous solution turns clear. During each decrement the particles was collected either directly from the flow output or a

second magnetic column with a strong magnetic of 0.22 T. The fractionations were collected until the aqueous solution turns clear. Then the magnetic field was reduced again to release multiple fractionations.

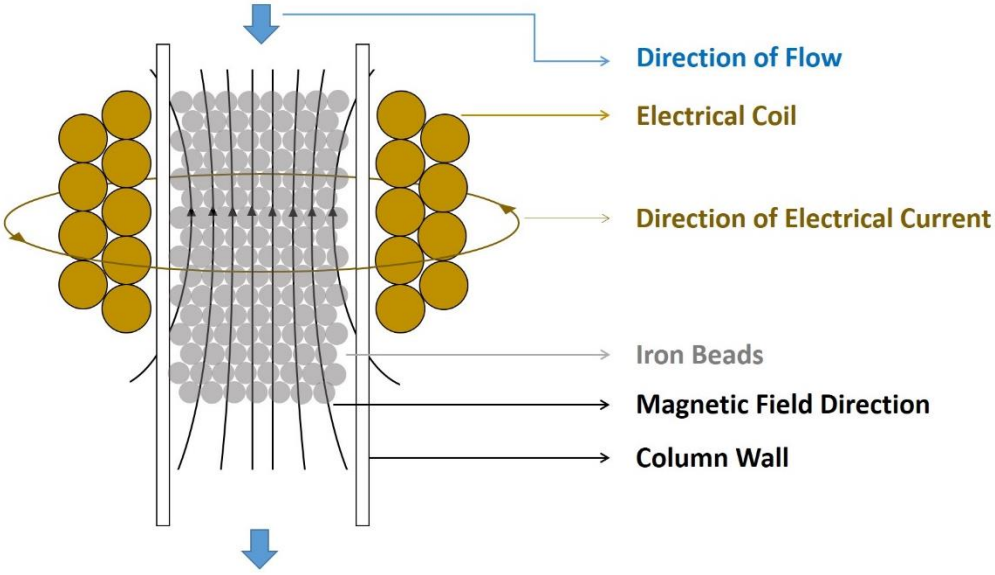

Figure 14, magnetic nanoparticle separation column.

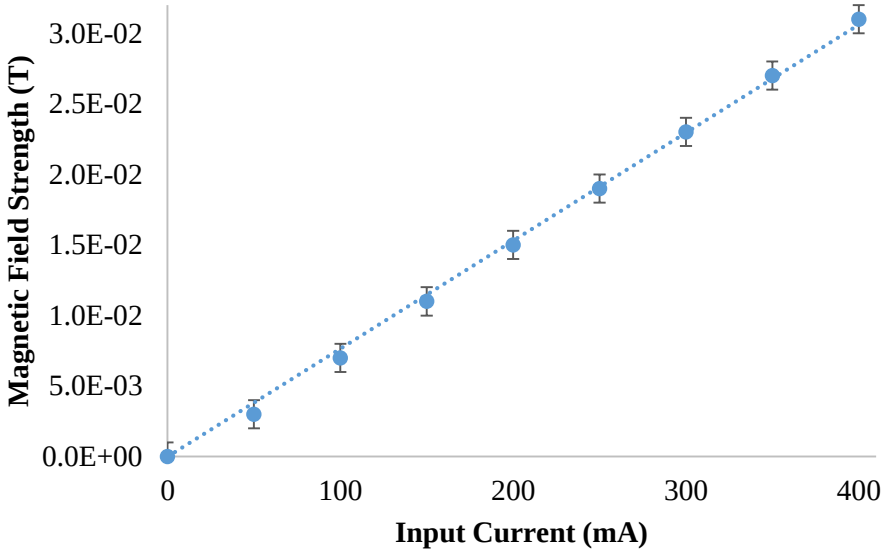

Figure 15, Magnetic field generated with different input current with a 22W electrical coil.

2.3: Performance comparison between DMF and MF techniques

2.3.1: Experiment

9 fractionations of both MF-SPIONs and DMF-SPIONs were produced from starch coated SPION solution with input current settings of 300, 200, 100, 50, 30, 20, 10, 5, 0 mA. Three runs of DMF and MF process were performed with a total of 54 fractionations. Both MF-SPIONs and DMF-SPIONs were sonicated for 2 minutes and measured for their sizes and size distribution by DLS measurements.

2.3.2: Results

Figure 16 showed a comparison of average particle size of starch coated DMF-SPIONs and MF-SPIONs under the same input current. Among the 54 fractionations, both the largest and the smallest average size fractions were obtained by DMF-SPIONs. Therefore, it indicated a wider separation range, as shown in **Figure 16**. More importantly, the DMF method significantly improved the PdI by an average of 55% in comparison to the MF method. The size distribution of all nine DMF-SPION fractions fell within the monodisperse range of PdI $\leq$ 0.1, as shown in **Figure 17**. The Malvern Instrument stated that a PdI value lower than 0.05 was usually only achievable with highly controlled spherical particles [111]. For example, polystyrene spherical nanoparticles were commonly used to calibrate the DLS performances and have a PdI value of 0.05. A PdI of 0.08 was an exciting result, since SPIONs are usually random shaped particles with collections of multiple iron oxide cores with an external matrix.

DMF was demonstrated to be a better separation method with a wider separation range and a narrower size distribution than conventional MF technique. Moreover, we found that the performance of DMF was strongly affected by the nature of PMF. Conventional MF method was considered as a DMF with 0 PMF cycle. With an additional 1 PMF cycle, the size

distribution of DMF-SPIONs was narrow down to a PdI value of 0.13 from 0.16 of MF-SPIONs. With additional 21 PMF cycles, the PdI of DMF-SPIONs can be further reduced to 0.08, as shown in **Figure 18**.

This study proves the effectiveness of the PMF on the particle size distribution. DMF showed a great size selection performance that has never been achieved before. Therefore, a series of experiments has been conducted to show that DMF is indeed effective, scalable and controllable.

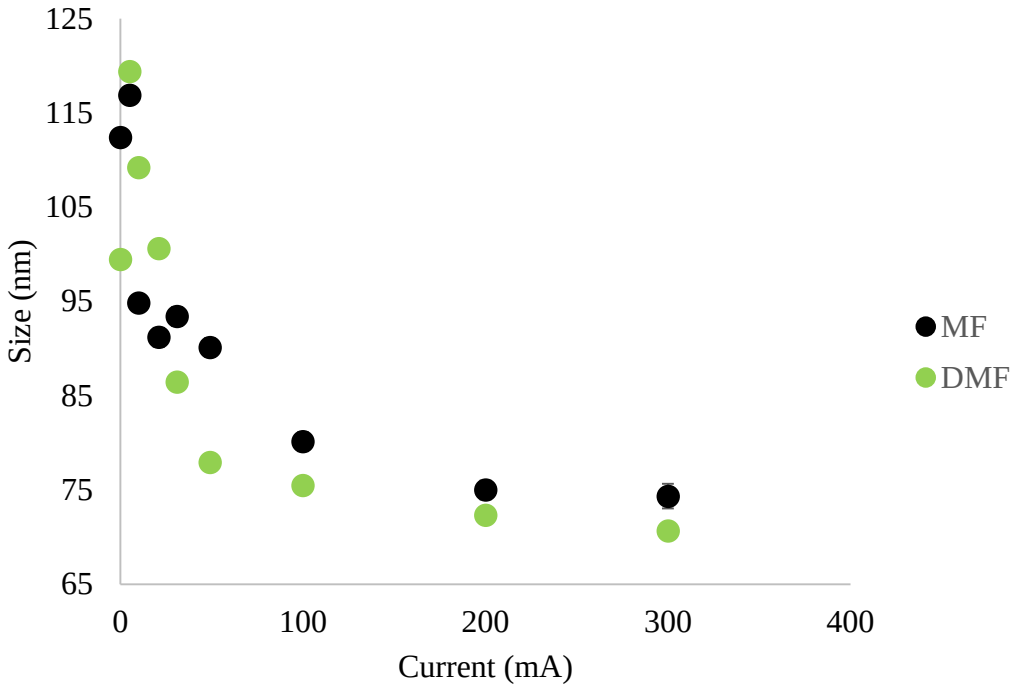

Figure 16. Starch coated SPIONs was separated by both MF and DMF techniques. The illustration showed a comparison of average particle size between both methods with their corresponding input current.

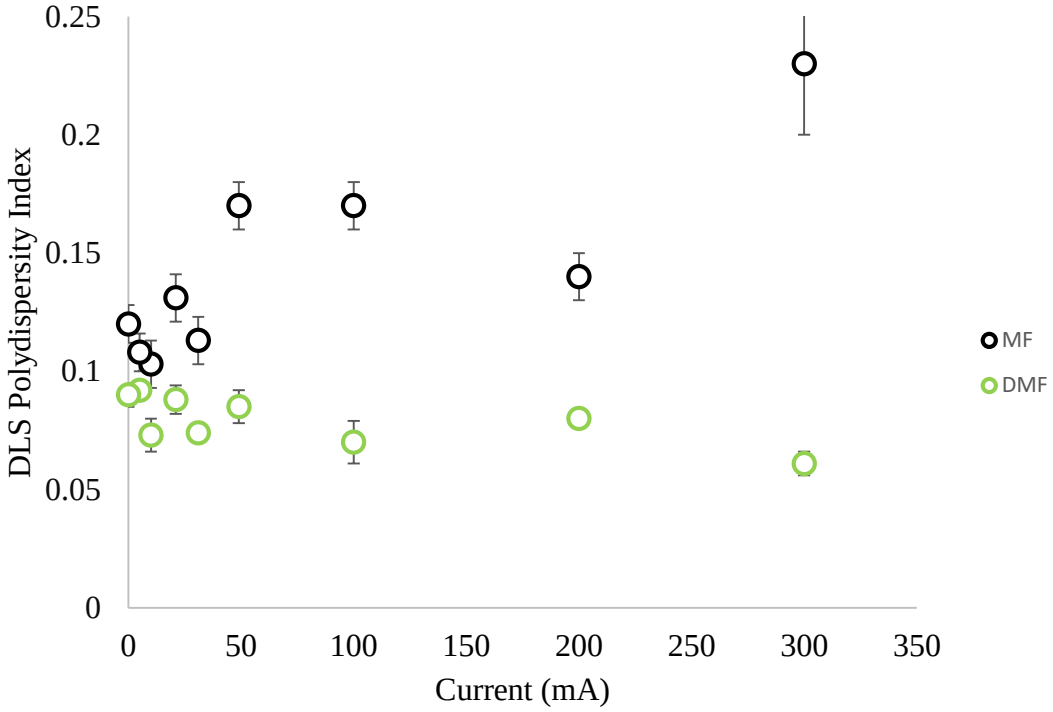

Figure 17. The illustration showed PdIs for both MF-SPIONs and DMF-SPIONs.

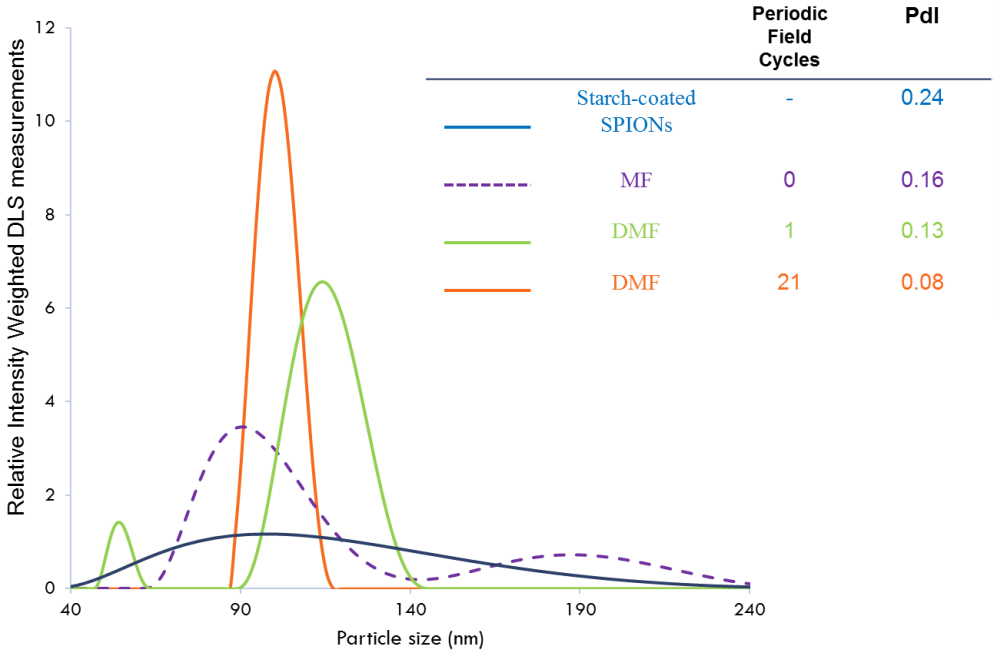

Figure 18. A plot of DLS measurements of starch coated SPIONs being separated with different periodic field conditions and their measured PdI values.

2.4: Automated DMF Setup

2.4.1: Introduction

The DMF method requires more time to process the same amount of particles in comparison with conventional methods, due to long duration of the PMF required. Therefore, a continuous and fully automated DMF process was proposed in this section to improve efficiency.

Figure 19 shows an automated DMF setup. Polydisperse SPIONs enter the system through particle inlet 1 and fill the column to the top location 2. The column is surrounded by electric coil 3, which is controlled by an AC or a DC power supply. AC supply is recommended in order to shorten the duration of the PMF. The magnitude and duration of the power supply are programed by a computer as shown in **Figure 19**. DMF-SPIONs will then be trapped by a second column 4 with a strong magnetic field provided by either an additional electrical coil or a fix magnet. DMF-SPIONs can then be extracted from the second column 4 with an aqueous solution or the entire second column 4 can be removed as a sample container. The entire process can be fully automated with the addition of an electrometer.

2.4.2: Experiment

The electrometer was used to measure the fluid resistivity and monitor the separation progress with the changes of the SPIONs concentrations. Triplets of 5 ml starch coated SPION solutions with concentrations of 0.05, 0.1, 0.15, 0.2, 0.25 mg Fe/ml were prepared. The SPIONs solution was circulated with a peristaltic pump and an open reservoir. A set of electrometer probes with 0.5 cm apart was installed in the water reservoir to measure the electro resistivity across the moving fluid.

2.4.3: Result and discussion

Figure 20 showed the change of electro resistivity with SPIONs concentration in the fluid. The experiment showed that the process of the DMF can be monitored by the SPIONs concentration in the fluid. Therefore, a computer can determine when to decrease the magnetic field and when to start another separation based on the reading of the electrometer. Once all DMF-SPIONs are captured in second column 4, the power supply will decrease the current output automatically and release larger DMF-SPIONs. Once the current reaches zero and all the particles pass through the system, new particles will be injected into particle inlet 1 and repeat previously described process for a new separation. The proposing automated process can be fully programed and operate the DMF accordingly. The process is proposed for large quantity separation. It was provisionally patented "62/251,951", and looking forward to a utility patent application.

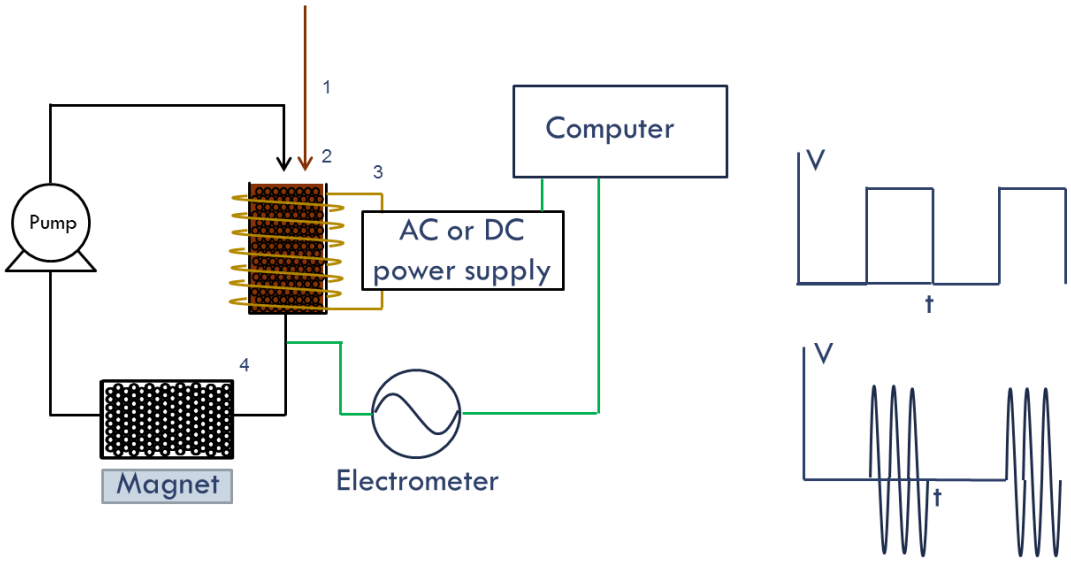

Figure 19. An illustrated diagram of a computer controlled continuous DMF setup.

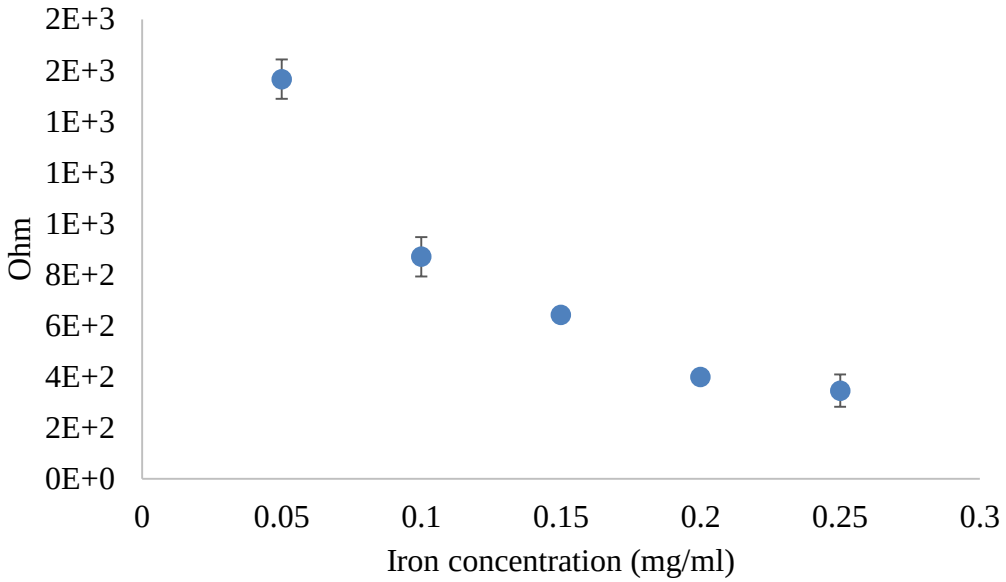

Figure 20. The electroresistivity change with different SPION concentration in aqueos solution.

2.5: DMF scalability

2.5.1 Introduction

Scalability is an important advantage of the DMF method for large quantity production of monodisperse SPIONs in low cost. There are many FDA approved or developmental biomedical applications based on SPIONs. The demand of SPIONs is expected to increase dramatically with time. Therefore, it is very meaningful to the medical industry to have a potential commercial solution for controlling the particle size distribution of SPIONs.

The DMF capacity is determined by two major parameters which are column volume and desired smallest fractionation size. The column volume is scalable by increasing radius or length of the column, as shown in **Figure 21**. According to Biot-Savart law, a larger column radius requires a larger current to maintain the magnetic field, and it results in rising of system temperature. A larger column length requires higher voltage to maintain the magnetic field, which is easier to achieve in an industrial facility comparing to current.

$$dB = \frac{\mu_0 I \overrightarrow{dL} \times \vec{r}}{4\pi R^2} = \frac{\mu_0 I dL sin\theta}{4\pi R^2}$$

$$B = \frac{\mu_0 I}{4\pi R^2} \oint dL = \frac{\mu_0 I}{4\pi R^2} 2\pi R = \frac{\mu_0 I}{2R}$$

The volume of the columns required is proportional to the amount of SPIONs being processed. To confirm the system scalability, the column was scaled up in length to five different volumes.

The desired smallest size to be fractionated will also affect the DMF capacity. The separation concept is based on moving the smaller SPIONs away from the magnetic source. Therefore, the DMF capacity is limited by the amount of the desired smallest size SPIONs that can be immobilized. The total capacity of DMF increases if the desired fractionation size is large. The required magnetic force of to immobilize a larger SPION is lower than a smaller one.

2.5.2: Experiment

The performance of the DMF was determined by its average PdI values of 4 DMF separations. The magnetic column was scaled into five different volumes by column length as shown in **Figure 21**. Three DMF runs and 21 PMF cycle were used to create 4 fractionations from starch coated SPIONs with input currents of 300 mA, 200mA, 100mA, and 0 mA. The DMF-SPIONs were collected and measured for their PdI values. The average PdI values were used to show the performances of different scaling volumes.

2.5.3: Results

Based on the average PdI values, the performance of the DMF remained unchanged regardless of the difference in volumes, as shown in **Figure 22**. The result indicated that the system had a linear scalability with volume and the performances were almost not affected. Combining the automation potential described in previous section, the DMF system has shown very high potential for industrial use. Therefore, the DMF is believed to be the solution for addressing the increasing demand for monodisperse SPIONs in medical industry.

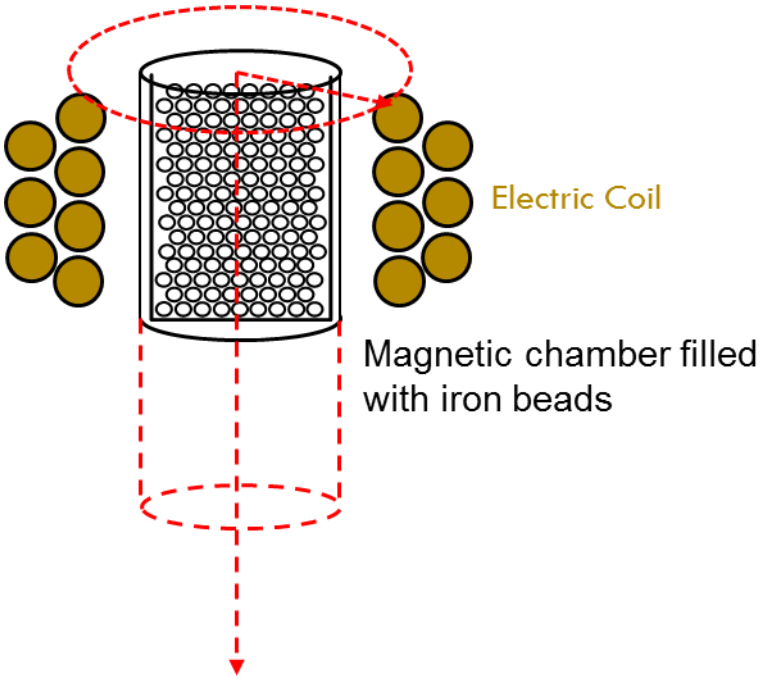

Figure 21. Illustration of potential scaling of column volume by column length and radius.

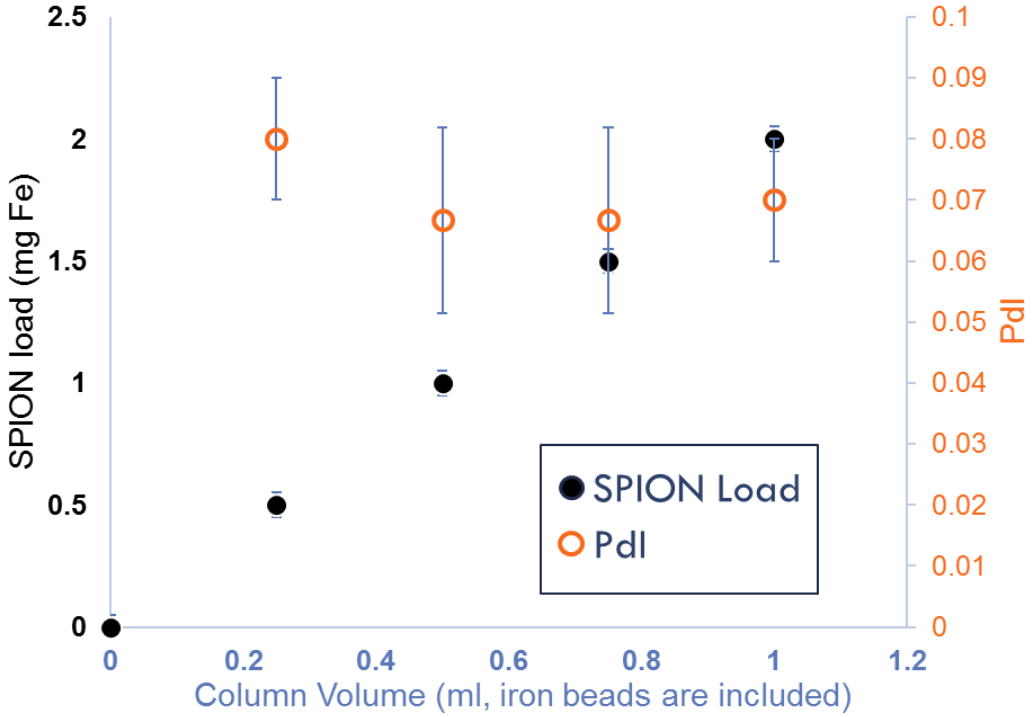

Figure 22. Illustration to show the scalability of DMF with 100 nm starch coated SPIONs and its corresponding PdI performance with different column volume.

2.6: DMF-SPIONs from SPIONs with different surface chemistry

2.6.1: Introduction

It is quite often to have surface modifications on nanoparticles in biomedical applications either to increase biocompatibility or to add special functions to SPIONs. Due to large surface to volume ratio of nanoparticles, there are significant inter particle interactions among particles, such as surface charge repulsion and steric repulsion of long chain polymers from modified surface. Therefore, it is essential to confirm the DMF performances on different modified SPIONs. We tested the DMF with different surface coated SPIONs including different surface charges and long chain polymer coatings.

2.6.3: Experiment

Starch coated SPIONs were cross-linked, aminated, and PEGylated according to previously described methods. Starch coated, aminated, and PEGylated SPION were size separated into 9 fractions by DMF. Three trials were performed on each SPION, and DLS was used to measure the size properties and PdI values. An average value of 27 DMF-SPIONs for each surface coated SPIONs was reported.

2.6.3: Results

Starch coated, aminated, and PEGylated SPIONs were prepared for this experiment. Starch coated SPIONs had an average size of 100 nm, PdI of 0.23 and an average Zeta potential of -9. Aminated SPIONs had an increase in average size and size distribution to 110 nm and 0.3 PdI value. The average zeta potential of aminated SPIONs is +40, which indicates a strong positive charge on surface. PEGylated SPIONs had further increased the average particle size to 145 nm, due to the long chain polymers. The particle size distribution was decreased to 0.15,

due to loss of smaller particles during the PEGylation process. The zeta potential was reduced to +20 from the aminated SPIONs, due to consume of amine groups.

The DMF process was performed on these SPIONs and the results were shown in **Figure 23**. Stronger magnetic field was required to immobilize the aminated SPIONs because of strong inter-particle repulsion and PEGylated SPIONs because of steric repulsion. Under same DMF conditions, starch coated SPIONs can be immobilized by only 150 mA of applied current while aminated SPIONs required 300 mA and PEGYlated SPIONs required 420 mA.

The result showed that DMF had the ability to overcome inter-particle interactions. Once the DMF process was activated by enough magnetic field, the separation process was considered to work well regardless of the difference in particle surface chemistries. However, extremely high current input may result in over-heating at the magnetic coil and damage the system.

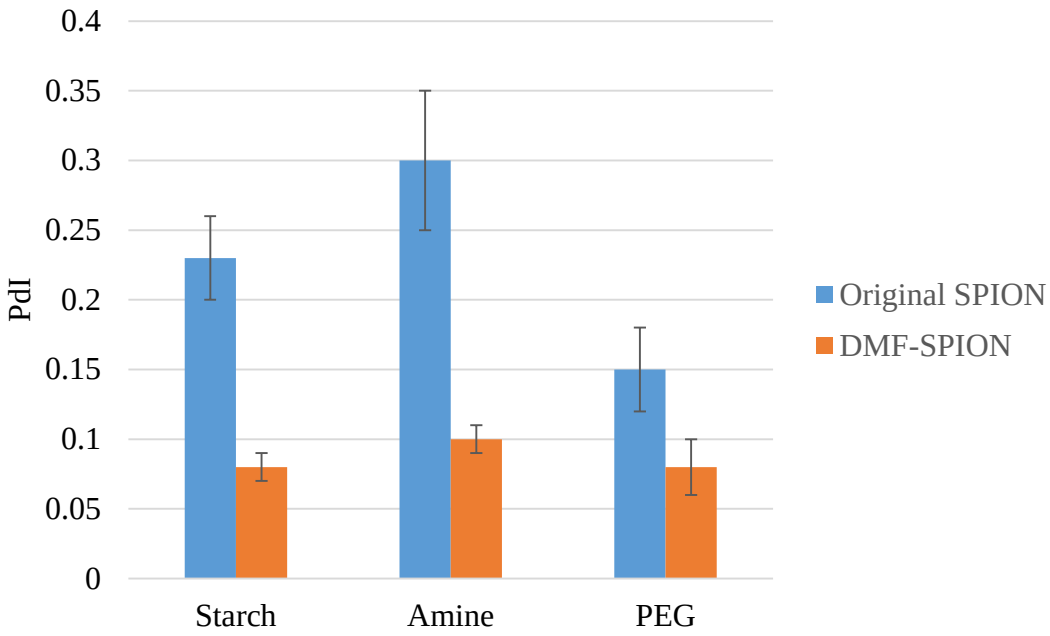

Figure 23. PdIs of different surface coated SPION and their DMF-SPIONs.

2.7: DMF for a surface modification process

2.7.1: Introduction

As described in earlier sections, DMF showed great performance regardless the difference in surface chemistry. However, surface modification process usually involves multiple steps with single starting material, leading to multiple intermediate products and resulting in single final product. There are three steps in surface modification to achieve PEGylated SPIONs, starting with starch coated SPIONs, followed with amination to generate aminated SPIONs. The aminated SPIONs were further modified to provide PEGylated SPIONs, as shown in the top of **Figure 24**. In order to optimize the DMF performance of surface modified SPIONs, a DMF process is performed on starting material and products from each surface modification step to verify the difference in results.

2.7.2: Experiment

Three DMF processes were performed on starch coated SPIONs, aminated SPIONs, and PEGylated SPIONs, which represented a starting material, an intermediate product and a final product respectively. The first DMF was performed on the starting material, starch coated SPIONs. The resulting separated starch coated SPIONs were further aminated and PEGylated without any further DMF treatment and labeled as P1. The second DMF started with the aminated SPIONs. The resulting separated aminated SPIONs were further PEGYlated without any additional DMF and labeled as P2. The third DMF was performed on PEGylated SPIONs and labeled as P3. An illustrated diagram of the experiment is shown in **Figure 24.**

2.7.3: Results

P1 and P3 showed similar performance, while P2 showed a significant higher PdI value as shown in **Figure 25**. There are no much differences for DMF to be performed on the starting material or the final product. Therefore, it is preferred to perform DMF on the starting material to prevent the waste of expensive coating material.

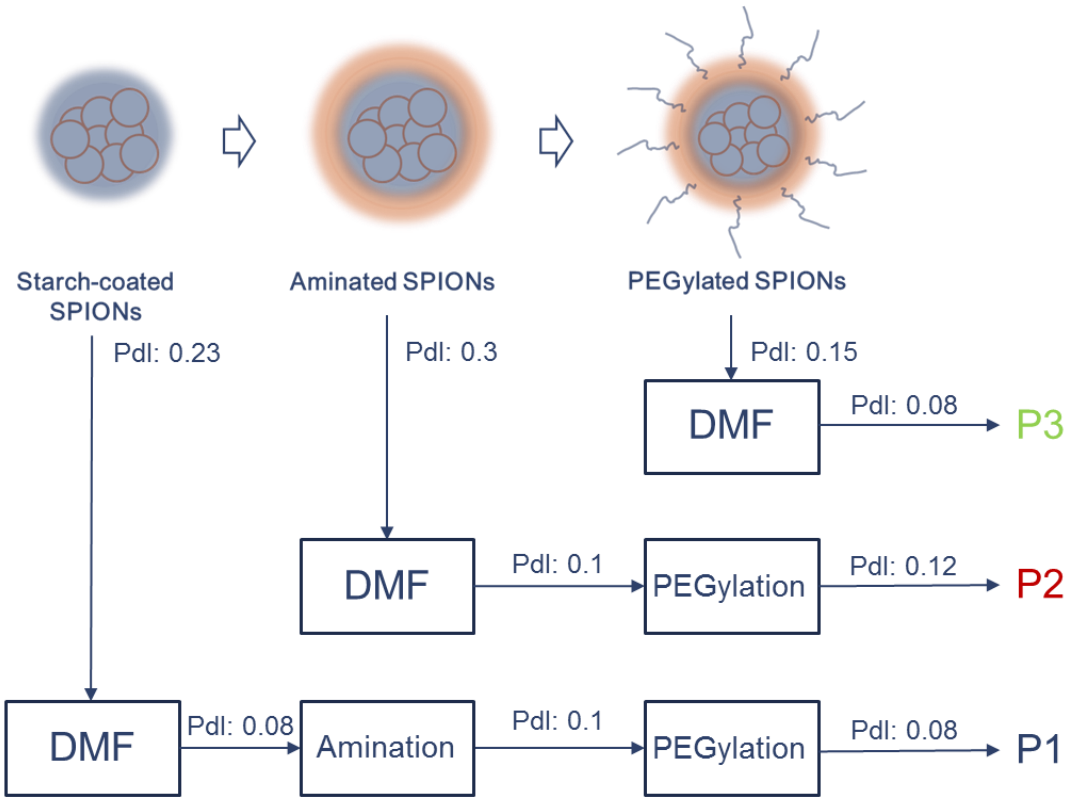

Figure 24. A diagram for the process PEGylation and DMF for P1, P2, and P3 DMF-SPIONs. The PdI value of each intermediate product are listed.

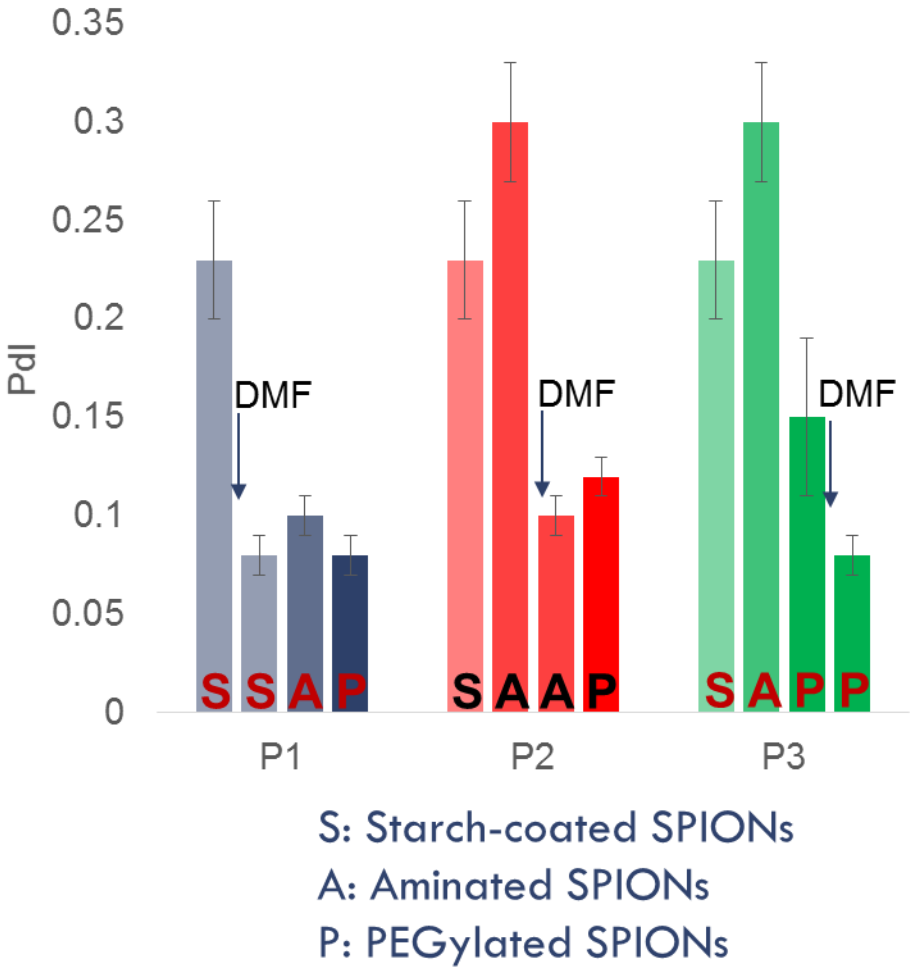

Figure 25. PdI measurements for the final products of P1, P2 and P3 DMF-SPIONs.

2.8: SPIONs recovery efficiency of DMF process

2.8.1: Introduction

The DMF process was demonstrated to have excellent performance and scalability as a size separation solution in comparison to any conventional method. The SPIONs recovery efficiency is evaluated by comparing the collected mass of DMF-SPIONs to the mass of original SPIONs. Starch coated SPIONs in 100 nm were used in this experiment to evaluate the DMF-SPION recovery efficiency.

2.8.2: Experiment

Starch coated DMF-SPIONs were obtained as described previously. The DMF-SPIONs were measured for sizes and size distributions by DLS and their iron content with Ferrozine assay. The iron mass from each DMF-SPION fraction was estimated with the Ferrozine assay and used to create a mass weighted size distribution. The mass weight size distribution can be used as a relative volume weighted size distribution with an assumption of constant density. The volume weighted average size distribution can then be compared to the volume weighted DLS measurement of the original starch coated SPIONs before the DMF process.

2.8.2: Results

Throughout the DMF process, nine fractionations were collected from a starch coated SPIONs with a total iron mass of 0.4 mg, volume weighted average size of 89.7 nm and a PdI value of 0.18. The DMF-SPIONs had a combined total iron mass of 0.38 mg, and mass weighted average size of 90.8 and a PdI of 0.09.

Under constant density, mass is in proportionality to volume. Therefore, volume weighted DLS measurement was used. The DMF-SPIONs results indicated 95% in recovery

efficiency by mass and an average size very close to the original SPIONs, as shown in **Table 2**. Almost all of the original SPIONs were recovered after the DMF treatment with very narrow size distributions in each fraction. The volume weighted size distribution of the original SPIONs can then be estimated from the DMF-SPIONs. The size distribution of the DLS measurement was made under an assumption of normal distribution. Therefore, the size distribution from recovered materials was considered to be closer to the actual size distribution of the original starch coated SPIONs, as shown in **Figure 26**.

Our experiment has demonstrated that the DMF process is a very efficient method with as high as 95% recovery efficiency from the original starch coated SPIONs. In addition, the overall average size remained unchanged before and after the DMF treatment. Therefore, we can say the DMF separation results in efficiency. In the following chapter, a mathematical model will be introduced to help in explaining and predicting the DMF results.

Size (nm)	Input Current (mA)	Iron mass (± 5% mg)
70.7 ± 1	300	0.01
72.3 ± 1	200	0.00
75.5 ± 1	100	0.07
78 ± 3	50	0.1
86.4 ± 2	30	0.07
100.6 ± 1	20	0.04
109.2 ± 1	10	0.04
116.9 ± 1	5	0.02
100.3 ± 1	0	0.03
Total mass	**0.38 mg (95% recovery efficiency)**	
Average size	**90.8 nm**	
Original size	**89.7 nm**	

Table 2. Evaluation of recovery efficiency of DMF with 100 nm starch coated SPIONs.

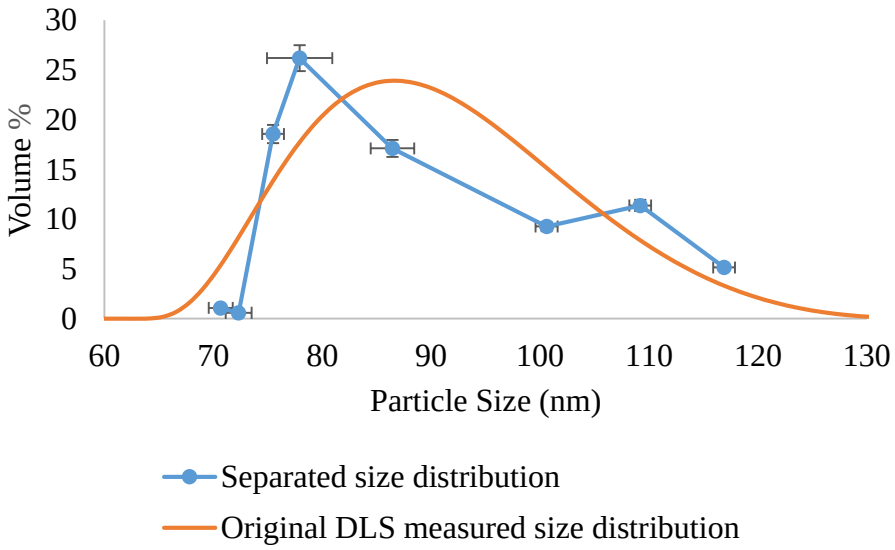

Figure 26. A comparison of 100 nm starch coated SPION size distribution estimated from DMF-SPIONs with their original starch coard SPIONs.

2.9: Theory and system modeling

We had proved that the DMF process is a very efficient and scalable process. The DMF process can also produce different monodisperse DMF-SPIONs by changing the input current or change to different coil if needed. In order to optimize the system capacity and the critical current for each fractionation, it can be time consuming and cost lots of materials to obtain a desired DMF conditions. Therefore, we are proposing a mathematic model to predict and control the DMF behaviors.

Mathematic and physic theories were used to confirm the mechanism of the separation process. The DMF immobilized SPIONs with a column packed with iron beads. The magnetic attraction force acted upon different size SPIONs was calculated based on the magnetic induction around a single iron bead. The general magnetic force can be calculated with the following relationship.

$$F_m = \nabla(m \cdot B)$$

In this mathematic model, F_m is the magnetic force, m is the magnetic moment of SPIONs and B is the magnetic induction from magnetized the iron beads. All of the iron beads were assumed to be spherical, and the magnetic potential ψ of a magnetized sphere can be modeled from the following equation [113].

$$\psi(r,\theta) = -H_0 r\, cos\theta + \sum_n (A_n r^n + B_n r^{-n-1}) P_n(r\, cos\theta)$$

In the equation, H_0 is the ambient magnetic field, A_n and B_n are related to the material magnetic permeability and boundary condition and P_n is the legendre function. H_0 was directly measured by a tesla meter (F.W. Bell, 5100 Series). The equation can be reduced to the following for an iron sphere.

$$\psi(r,\theta) = -\frac{M_0}{3} r\, cos\theta + \frac{M_0}{3}\frac{R_0^3}{r^2} cos\theta$$

In this equation, M_0 is the magnetization of the iron bead which is a function of H_0, as shown in **Figure 27**. Three magnetization curves were shown in **Figure 27** and represent three

directions of magnetization to a single crystal iron. In this case, the magnetization directions were fixed, and therefore represent three magnetization of three iron crystal directions. The crystal structure of the iron beads was unknown, and therefore all three magnetization curves were used in the model for comparison. Here R_0 is the radius of the iron bead which can be measured by the optical microscope with an average diameter of 147 μm, as shown in **Figure 28**. We can then calculate the magnetic field with the following equation.

$$\vec{H} = -\nabla\psi = \frac{\partial}{\partial r}\psi(r,\theta)\delta_r + \frac{\partial}{\partial \theta}\psi(r,\theta)\delta_\theta$$

The origin was set to be at the center of the sphere, and θ is the angle between the direction of the external magnetic field and the position of interest. Therefore, we were able to plot the total magnetic field H as shown in **Figure 29**. Further, the magnetic force equation was substituted to calculation magnetic force field as the following equation

$$F_m = \nabla\left(\frac{4}{3}\pi R_{np}^3 D\chi\vec{H}\cdot\mu\vec{H}\right) \cong \frac{4}{3}\pi R_{np}^3\mu^2(\frac{Mnp}{B})\nabla(H_r^2 + H_\theta^2)$$

Where $R_{np}$the radius of a nanoparticle, D is the density of the nanoparticle, χ is the magnetic susceptibility, μ is the magnetic permeability, M_{np} is the mass magnetization of the nanoparticle, H_r and H_θ are the r and θ components of the magnetic field. M_{np} of SPIONs can be estimated by fitting the Langevin function to the SQUID measurements as shown in **Figure 30**. Then the magnetic induction was obtained by $B = \mu H$, and F_m can be calculated as **Figure 31**.

A similar process was performed on the hydraulic drag force. The Reynolds number for the packed column can be estimated by the following equations. A Reynolds number of 12.5 was found for the DMF system.

$$Re_p = \frac{D_p V_s \rho}{(1-\varepsilon)\mu}$$

$$D_p = 6\frac{Volume\ of\ bead}{Surface\ area\ of\ bead}$$

We assumed Newtonian flow past a single sphere, and the velocity of the fluid flow was calculated with the following equations.

$$V_r = -V_0 cos\theta(1 - \frac{3R_0}{2r} + \frac{R_0^3}{2r^3}),$$

$$V_\theta = V_0 sin\theta(1 - \frac{3R_0}{4r} + \frac{R_0^3}{4r^3}).$$

Therefore, the fluid velocity field is as shown in **Figure 32**. The fluid drag force on a single SPION can then be estimated by Stoke's drag,

$$F_d = 6\pi\eta R_{np} V$$

where η is the fluid viscosity. A mapping of the drag force is shown in **Figure 33**. A combined result of magnetic force and hydrodynamic drag force is shown in **Figure 34**, where the intensity is calculated by the ratio of the magnetic force over the fluid drag force.

$$Intensity = \frac{Magnetic\ Force}{Fluid\ Drag\ Force}$$

An intensity value > 1 means that the magnetic force dominates the fluid drag force in the area, which will result in SPIONs to be immobilized. An intensity value ≤ 1 indicates that the fluid drag force is stronger than the magnetic force, which will result in SPIONs being free to travel and released from the system. Integration of all volumes with intensity value >1 results in an effective volume Ve. Ve is the maximum capacity of SPIONs on a single sphere at a specific input current and specific size. Therefore, Ve is a function of particle size and the input current. Therefore, we can model the Ve by the following equation based on an assumption of [1,1,1] crystal direction for the iron beads, where the black dots are the theoretical values and the color surface is the fitting equation.

$$Ve\ [1,1,1] = a + b \cdot \ln(y + c) + d \cdot (x - e)^{\ 3}$$

a = 0.117, b = 0.0519, c = 2.43d = 5.34e-9, e = -249

Where for the presented function the fit had $R^2 = 0.93$. The relationship is shown in **Figure 35**, where area below the color surface indicates SPIONs to be immobilized due to the domination of the magnetic force. On the other hand, area above the color surface indicates

SPIONs are free to release. The same process applied to [1,1,0] iron crystal direction, as shown in the following equation and **Figure 36**.

$$Ve\ [1,1,0] = a + b \cdot \ln(y + c) + d \cdot (x - e)^{3}$$

a = 0.177, b = 0.0326, c = 0.13, d = 3.93e-9, e = -320

For [1,0,0] iron crystal structure, the theoretical result could not fit into the same model, as shown in **Figure 37**. The [1,0,0] crystal structure indicates the separation will not happen, because all the particle will either be immobilized or released at once. The relative volume was measured, as shown in **Figure 26** in the previous section, but the actual Ve for the immobilized SPIONs was unknown. The first fractionation of the experiment involved SPIONs that were not captured with the highest magnetic field, which does not apply to our mathematic model. Therefore, the second fractionation data was used to determine the Ve for the system. The second fractionation had an average size of 72.32 nm and was released from a change of input current from 300 mA to 200 mA. We can estimate the Ve at 300 mA and 200 mA separately with the Ve modeled equation and calculate the total Ve for the system with the known relative volume. Thus, the Ve of each data point can be calculated and combined with the known average size from each separation. We can then determine the theoretical input current for each fractionation to happen from the fitted equations. We can then compare the theoretical estimates with the experimental, as shown in **Figurer 38**. The experimental result agrees very well with the theoretical value calculated from the [1,1,1] crystal directions.

The experimental results showed a very close relationship to the theoretical plot with assumptions of no diffusion and mono-crystal structure of the iron beads. The model requires the magnetic susceptibility of the particle which can be measured by SQUID with a small amount samples which can be reused. A test run of DMF is required with at least three separations. After the test run, the model can be used to calculate the input current setting for different DMF separations with different desired average size. The model have room for further improvement by other fitting equations. In the future, a better understanding of the equation

will be developed by connecting the theoretical result to its physical meaning. Then, the model can be applied to different SPIONs with different physicochemical properties without the need of the DMF test run.

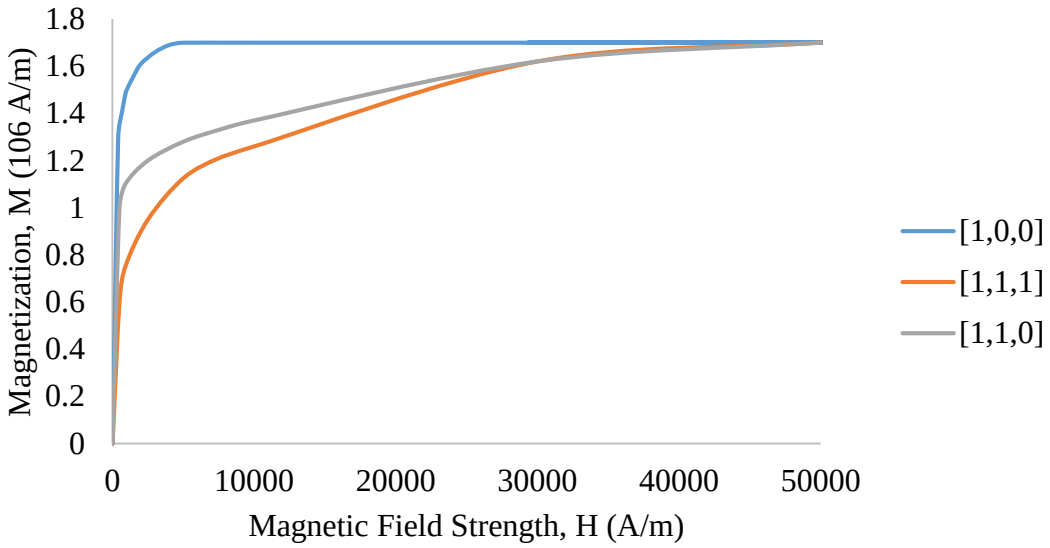

Figure 27. Iron magnetization curve for single crystal in [1,0,0], [1,1,1] and [1,1,0] directions. Miller indices are used for different crystal directions.

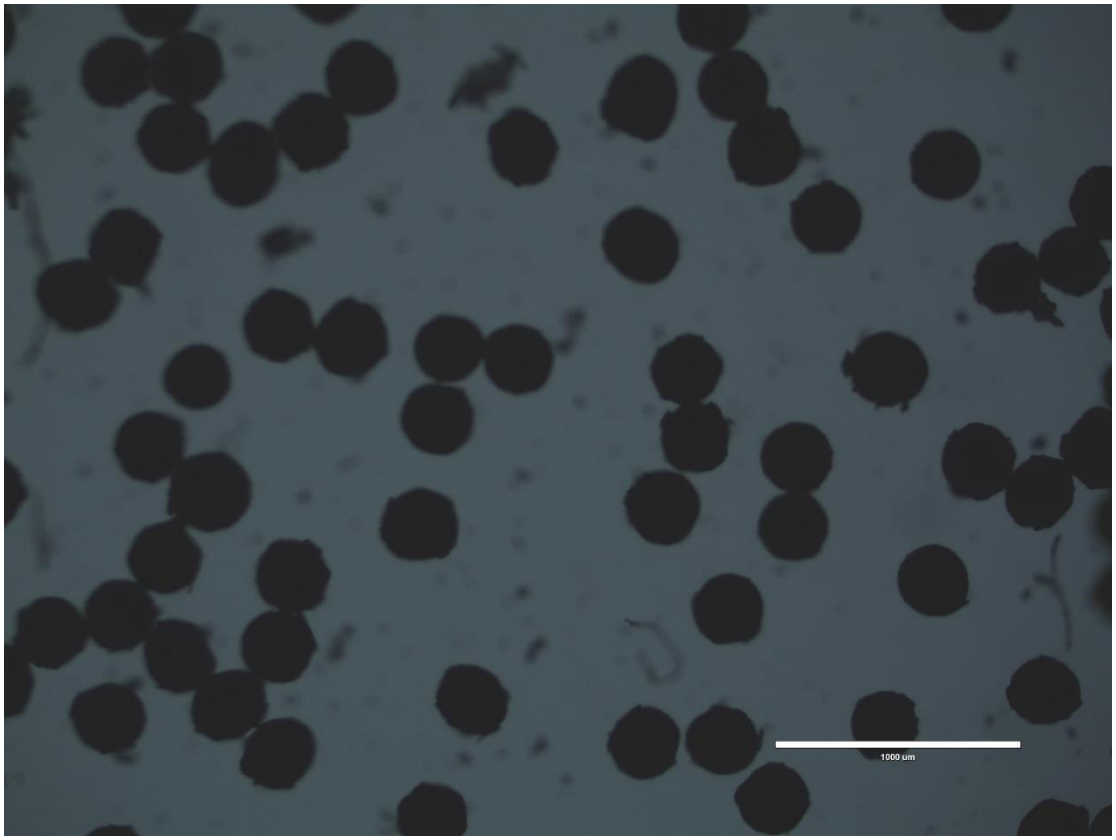

Figure 28. Iron beads under optical microscope.

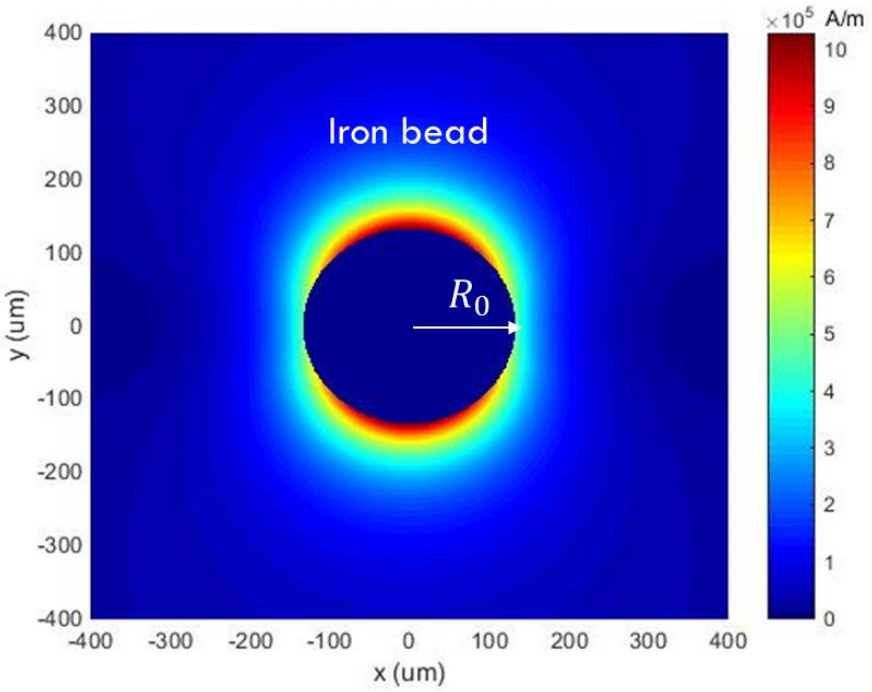

Figure 29. Scalar magnetic potential of a single iron bead.

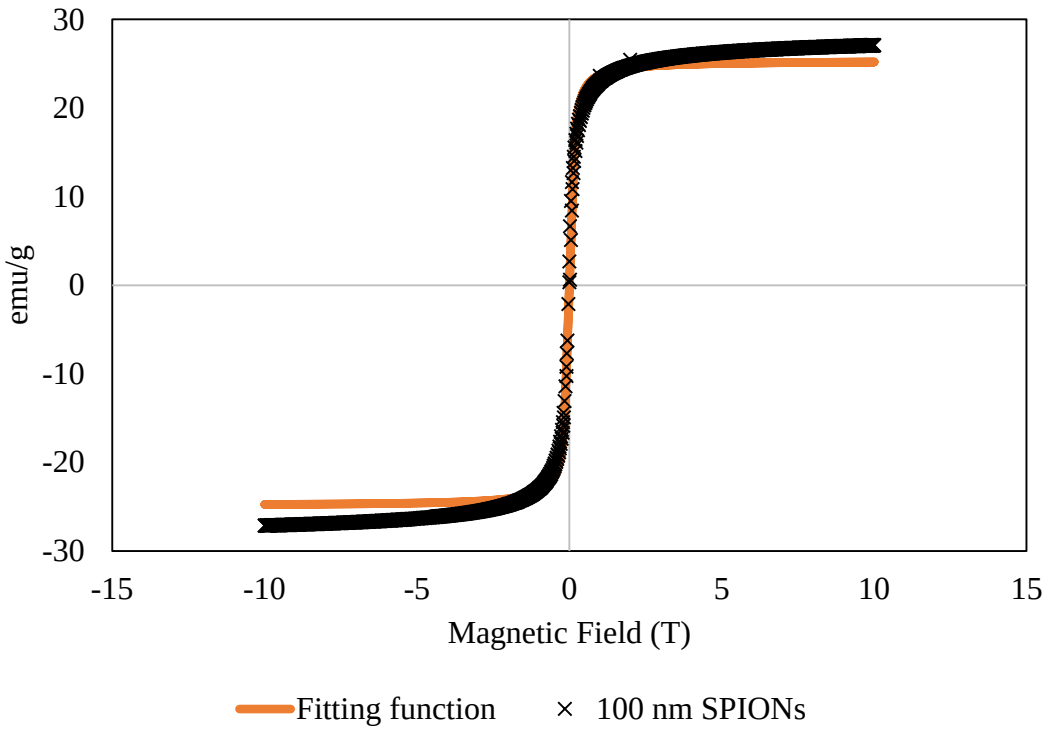

Figure 30. A Langevin function fit to a SQUID measurement of 100 nm starch coated SPIONs.

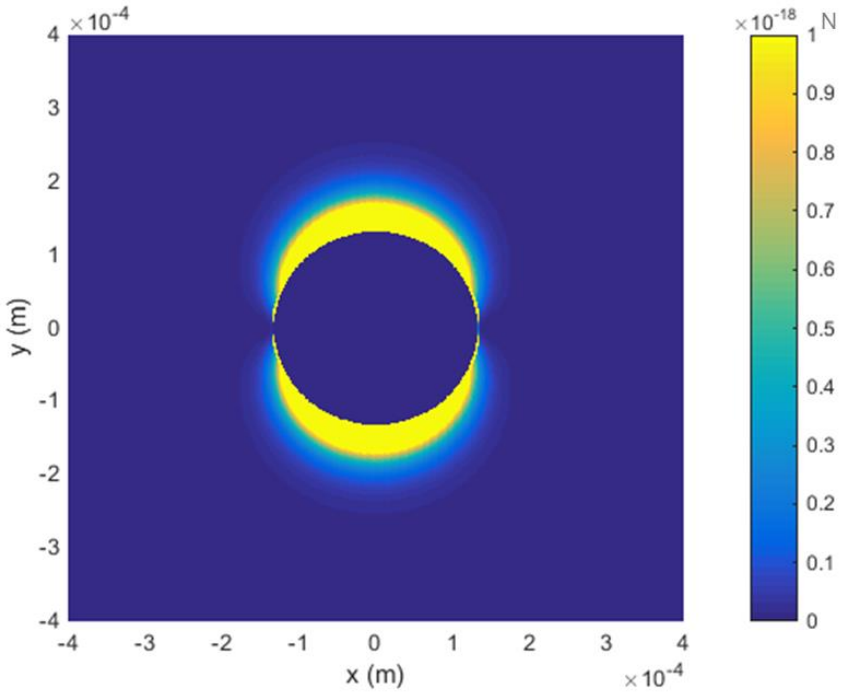

Figure 31. Magnetic force field of a single iron bead.

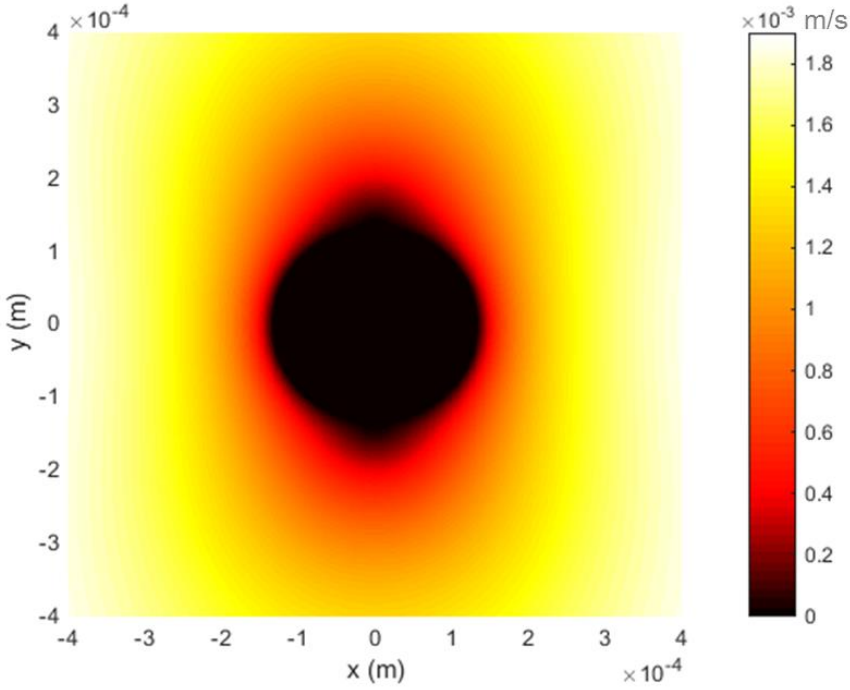

Figure 32. Fluid flow past a sphere with a Newtonian flow.

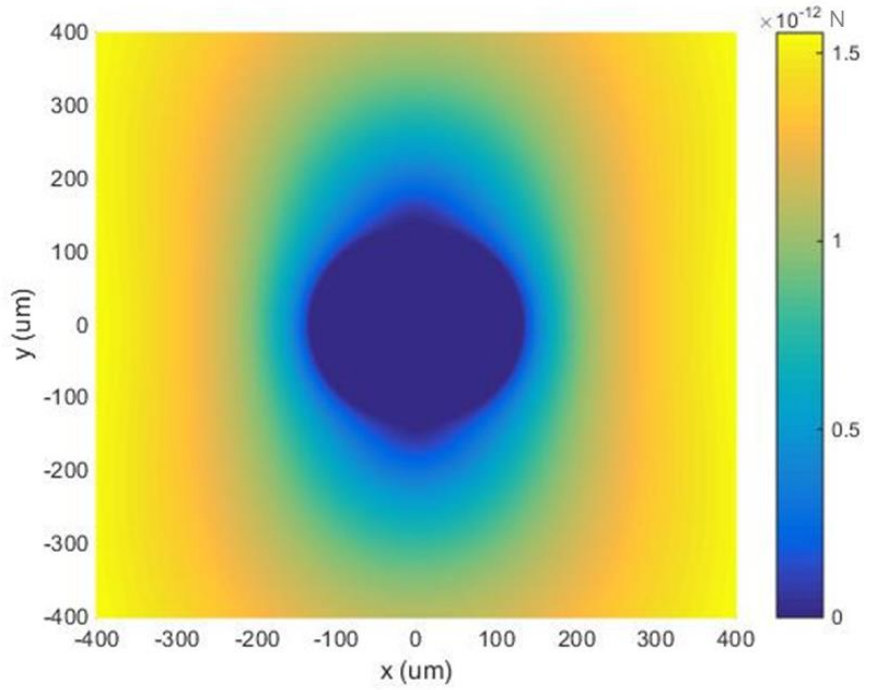

Figure 33. Hydrodynamic drag force on SPIONs past an iron sphere.

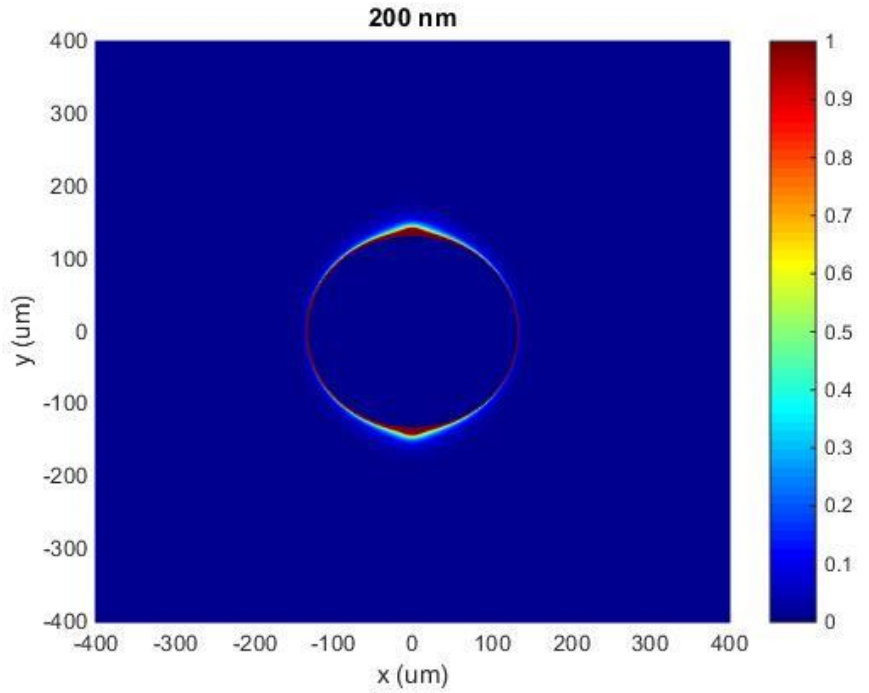

Figure 34. Illustration of an image of magnetic force / fluid drag force around a single iron bead.

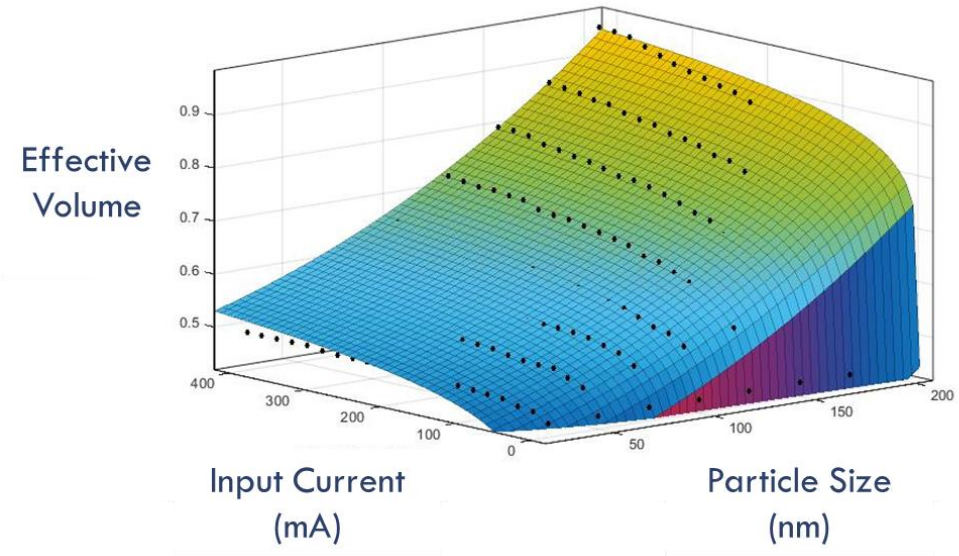

Figure 35. 3D illustration of the effective volume (Ve) with input current (mA) and particle size (nm) with a single iron sphere with a [1,1,1] crystal direction.

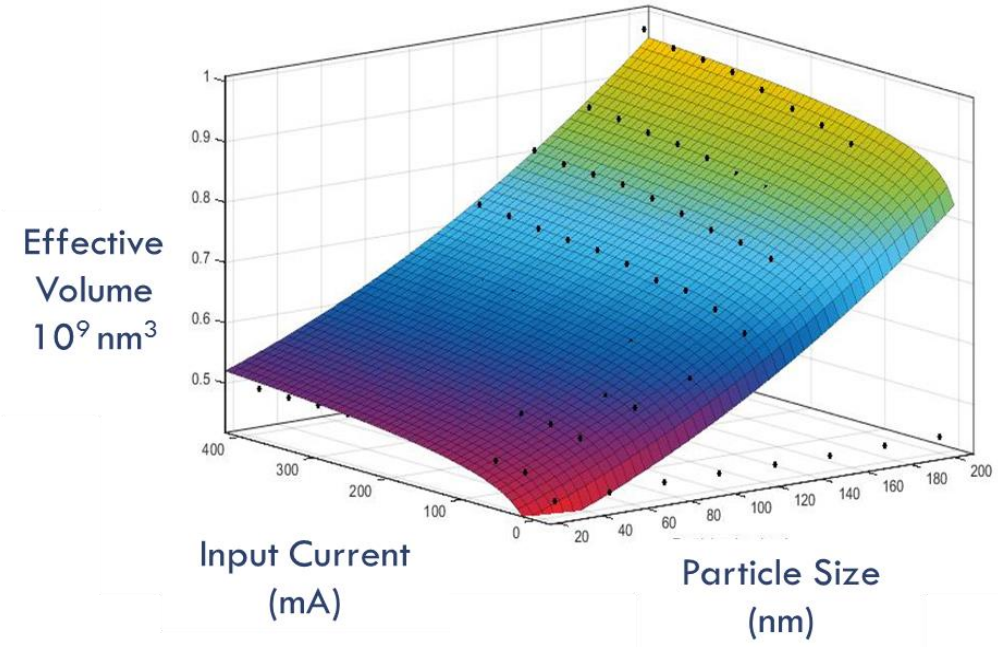

Figure 36. 3D illustration of the effective volume (Ve) with input current (mA) and particle size (nm) with a single iron sphere with a [1,1,0] crystal direction.

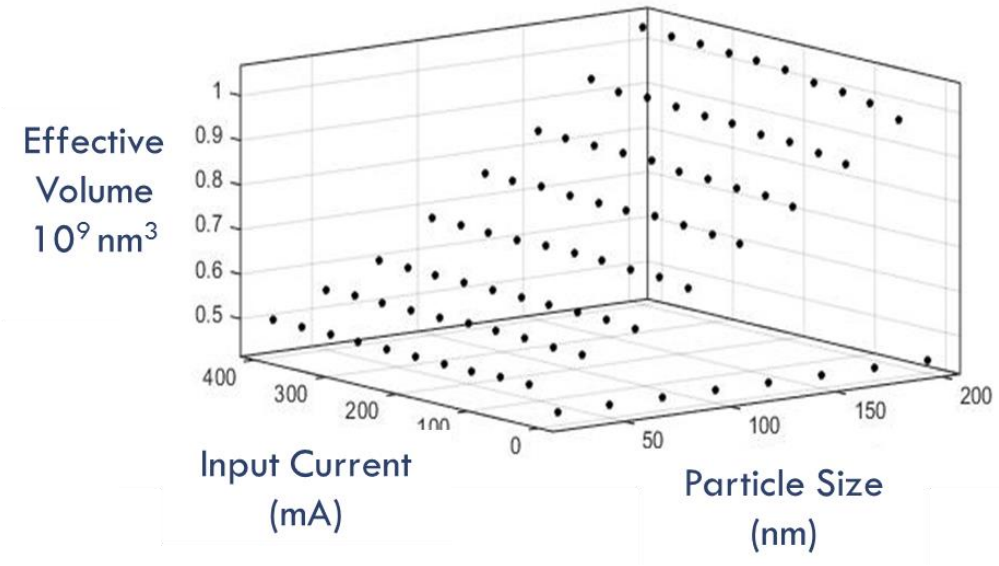

Figure 37. 3D illustration of the effective volume (Ve) with input current (mA) and particle size (nm) with [1,0,0] crystal direction.

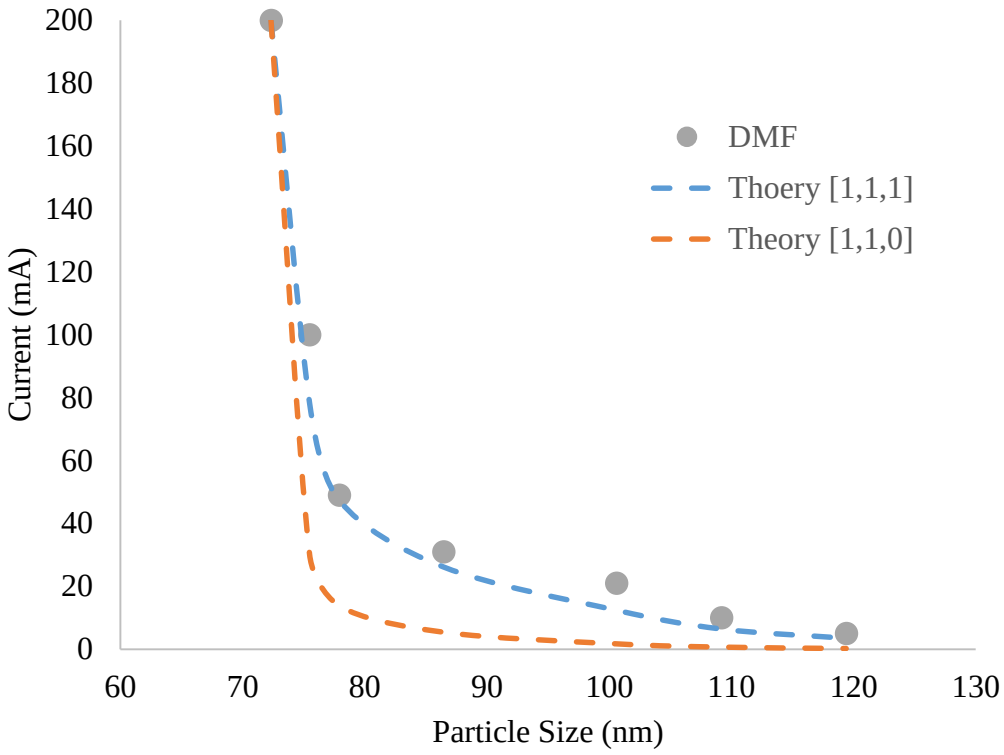

Figure 38. Theory vs experimental plot of 100 nm starch coated DMF-SPIONs and the theoretical result with a [1,1,1] and [1,1,0] crystal direction.

2.10: Application of monodisperse SPIONs

2.10.1: Introduction

In general, polydisperse SPIONs show random bio-distribution, MRI enhancement and low energy transformation. The effect of particle size was intensively studied by many researchers, but the effect of size distribution was mostly ignored. The main reason is because of the limited technology in controlling and obtaining samples with different size distribution for study. None of the existing techniques were able to produce monodisperse SPIONs. Now, the presented DMF technique enables us to have a closer look to the behavior of monodisperse SPIONs.

SPIONs behavior can be controlled with an external magnetic field. Unlike static magnetic field, alternating or rotational magnetic field tends to make SPIONs stay in suspension. The phenomena was related to the particle-particle interaction of SPION [64]. On the other hand, a polydisperse sample has a very different behavior from a monodisperse sample, for examples, SPIONs and DMF-SPIONs.

2.10.2: Experiment

The experiment was set-up as in **Figure 39**, where 50 µl SPION or DMF-SPIONs was introduced to the top of the 1 µm membrane with cell culture media solution (CCM). On the other side of the membrane, CCM of 200 µl was filled without any particle. There was a rotational magnet outside the bottom of the set-up to provide a rotational magnetic field with controlled rotational speed. CCM showed a better penetration in comparison to water or PBS (Phosphate Buffered Saline). A100 µl solution was taken out and replenished with the same amount of fresh CCM at each designated time period. Iron content was measured by ferrozine assay to assess the particle penetration profile for every taken sample.

Furthermore, the system was optimized by tuning the strength and the rotational speed of the magnetic field as shown in **Figure 40** and **Figure 41**. PEGylated SPIONs with the molecular weight of 5K were selected for this experiment because of its superior penetration profile.

2.10.3: Result:

DMF-SPIONs exhibited a significant increase in penetration in comparison to SPIONs. DMF-SPIONs showed a 90% penetration in 2 hrs while SPIONs showed 70% penetration under the same condition, as shown in **Figure 42**. **Figure 42** also indicated that SPIONs can form and de-form inter-particle structures with different rotational magnetic field. The actual inter-particle mechanisms remain unknown. However, our exciting preliminary results showed that the monodisperse DMF-SPIONs behaved very different from polydisperse SPIONs. It means that current SPION related technologies is indeed missing an important factor.

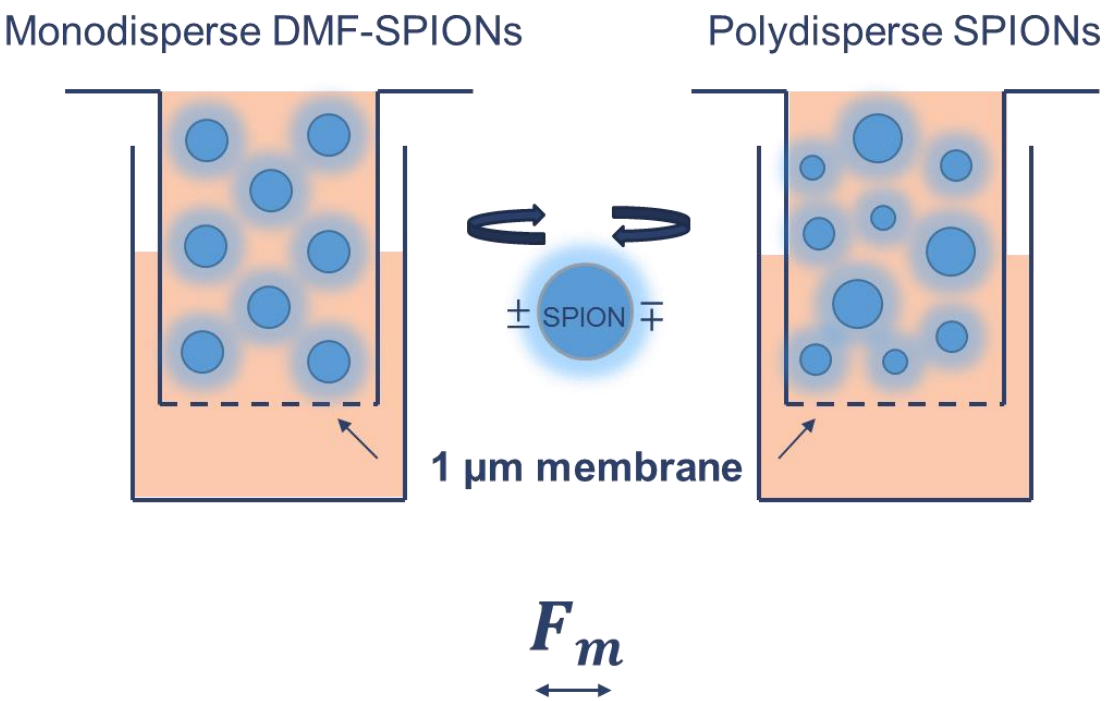

Figure 39. Experimental setup of SPIONs penetration study through a 1µm membrane with a rotational magnetic field.

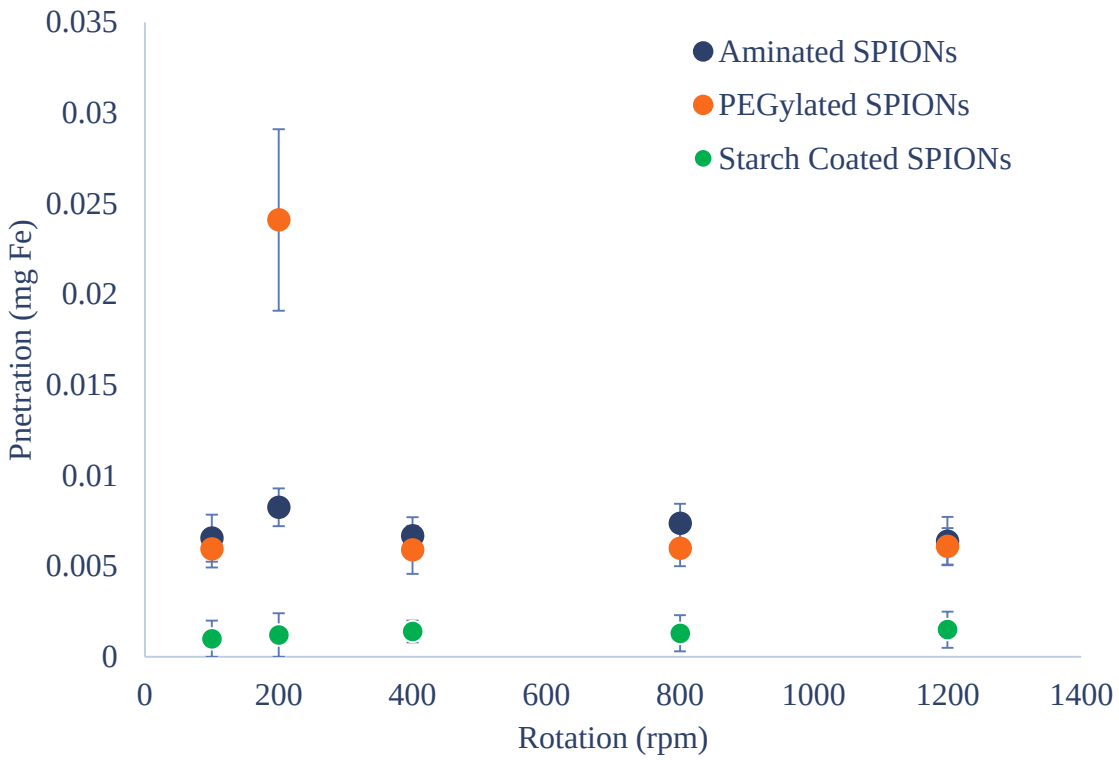

Figure 40. A Plot the amount of SPION penetration with different rotation speed and different surface coating.

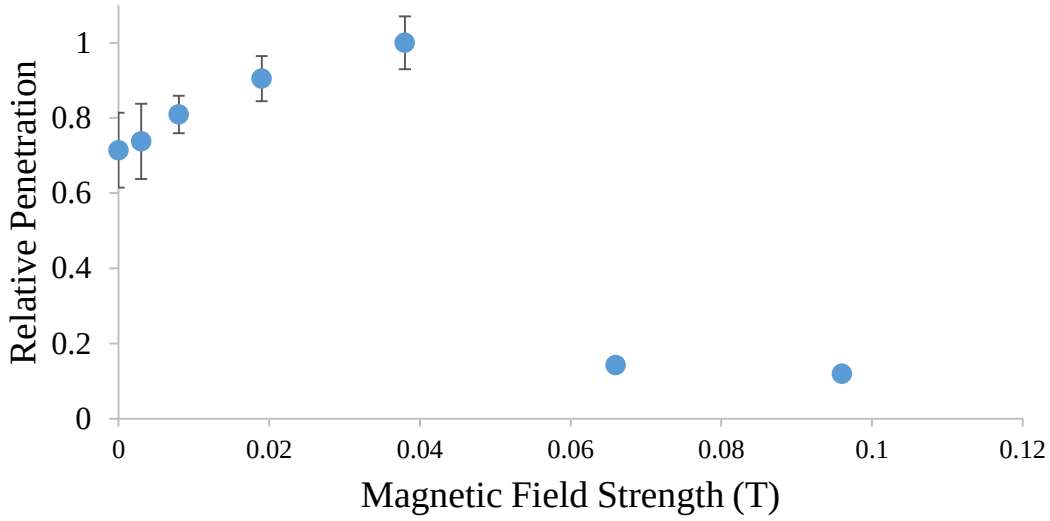

Figure 41. SPION penetration with different magnetic field strength with a 200 rpm rotational magnetic field.

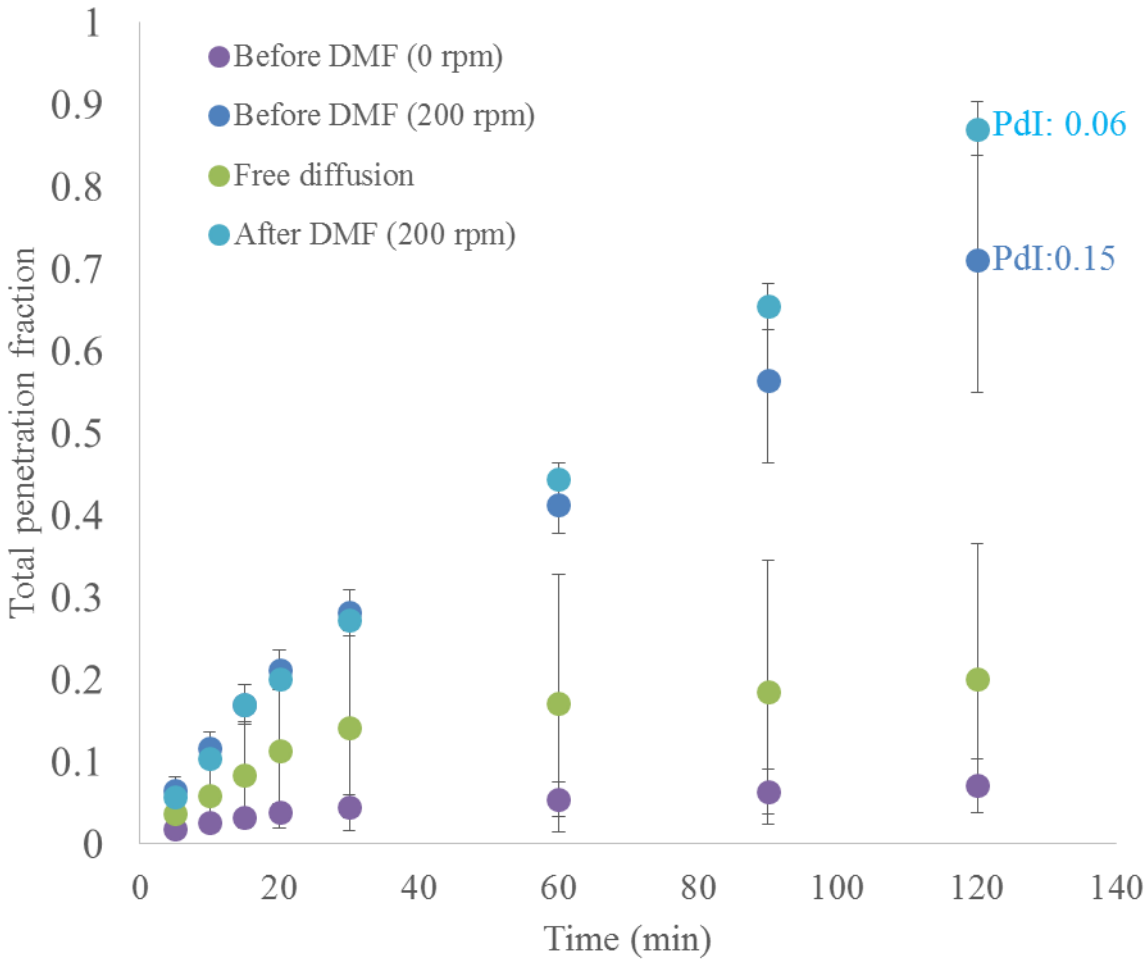

Figure 42. PEGylated SPIONs penetrated through 1µm membrane with a rotational magnetic field of different frequencies. Free diffusion indicates SPIONs penetration without any magnetic field.

2.11: Conclusions of size homogeneity

SPION is one of the most powerful nanoparticle because it has both magnetic property and biocompatibility. In comparison with other nanomaterials, multiple SPION based particles were FDA approved for different usages, such as AMI-225, Feridex or Resovist. However, the undesired size effects and inconsistent performances limit the adoption of this technology. Broad size distribution of SPIONs is the root cause for all the concerns. Therefore, many researchers turned away and looked for other nanomaterials with controllable size distribution, such as gold and silica nanoparticles. However, none of the material is able to provide the same advantages of SPIONs. That is why we focus on developing a solution, DMF method, to narrow down the size distribution of SPIONs. We have demonstrated that DMF is an efficient, controllable and scalable size separation method. It enables the preparation of monodisperse SPIONs with size distribution of $\sigma \leq 5\%$ and $PdI \leq 0.1$ which is unachievable by any other conventional methods. The DMF has also been proven to work for SPIONs with different surface chemistry and inter-particle interactions. We believe our innovation will bring SPION applications into a whole new level with a more controllable target delivery, more consistent MRI enhancement and better energy transformation in the near future. The monodisperse SPIONs can form or de-form inter-particle structures through external control. It will open up lots of potential applications in a totally new dimension, for examples, in controlling and releasing drug treatment as commended through external energy,

2.12: Future Work – Improvement of surface chemistry homogeneity of SPIONs

2.12.1: Introduction

All nanoparticle applications in biomedical field involved certain ways of delivery. It usually delivers drug or energy for medical treatment or the particle itself for imaging. However, the efficiency of the delivery was considerably low. In most cases, only 5% is able to reach the targeted biological entity. The remaining 95% of the nanoparticles was usually cleared out by different biological systems or just never had a chance to reach to the targeted area [32]. Therefore, countless researches invested on seeking a better way to improve the circulation time of nanoparticles. Among all physicochemical properties, the surface chemistry is the most important factor for circulation time of nanomaterials. Different coating systems were tested for an optimal solution for its application. Regardless of different synthesis methods, the product was always a combination of uncoated, slightly coated and fully coated particles. Different degree of modification results in particles with very different circulation. That is also the key reason for many synthesis methods which results in different circulation time for the same product. Therefore, we are suggesting a separation process to separated particles with different surface chemistry and generate homogenous products by their surface chemistry.

2.12.2: Experiment

SPION particles are used very often for their magnetic property. SPIONs with different surface coatings were separated by their size before the surface selection process; so each SPION sample has the same average size. Starch coated, aminated and PEGylated particles were used in this experiment as three different surface coatings. Each of them was separated with DMF by size to generate three samples with an average particle size of 100 nm. Then these particles were mixed together to represent a very broad surface chemistry distribution.

The mixture was then separated with DMF at three different magnetic fields. Zeta-potential was measured before and after the separation to show the difference in surface chemistry, as shown in **Table 3**. The Zeta potentials of the original SPIONs, mixture and the separated samples are shown in **Figure 43**, **Figure 44** and **Figure 45** respectively.

2.12.3: Results

The result showed that different surface coating could be separated by balancing the hydrodynamic drag force and magnetic force. Even though more experiments needed to be done to confirm surface chemistry from the result, our preliminary results have shown great value to the possibility of recycling unmodified or slightly modified SPIONs for further reaction and purification of the production for a long circulation time.

Surface	Zeta potential (mV)	Zeta potential after separation (mV)
PEG	+20.05	+23.95
Amine	+39.1	+40.83
Starch	-10.14	-9.35
Mixture of three (1:1:1)	-0.93	

Table 3. Zeta potential measurements of SPIONs before and after the surface separation process.

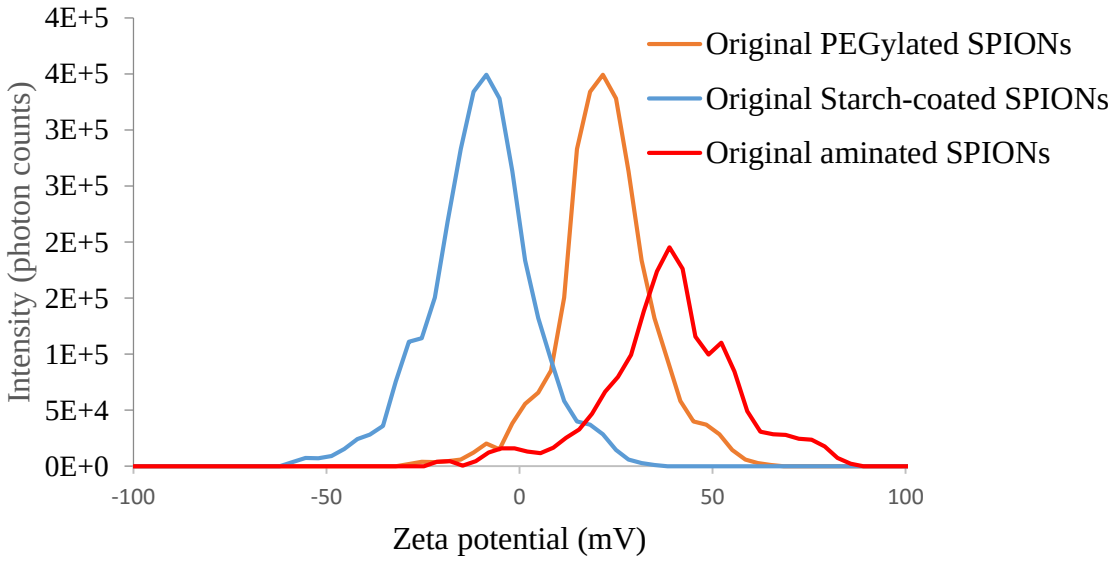

Figure 43. Zeta potential measurement of the original PEGylated, starch coated and aminated SPIONs before surface separation process.

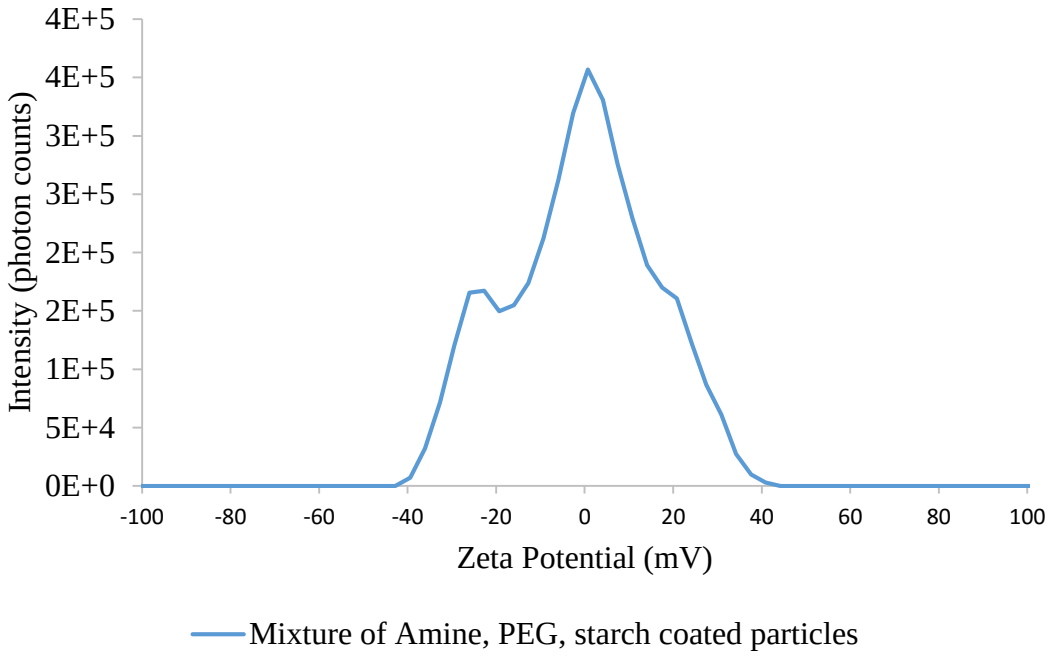

Figure 44. Zeta potential of 1:1:1 mixture of aminated, PEGylated and starch coated SPIONs

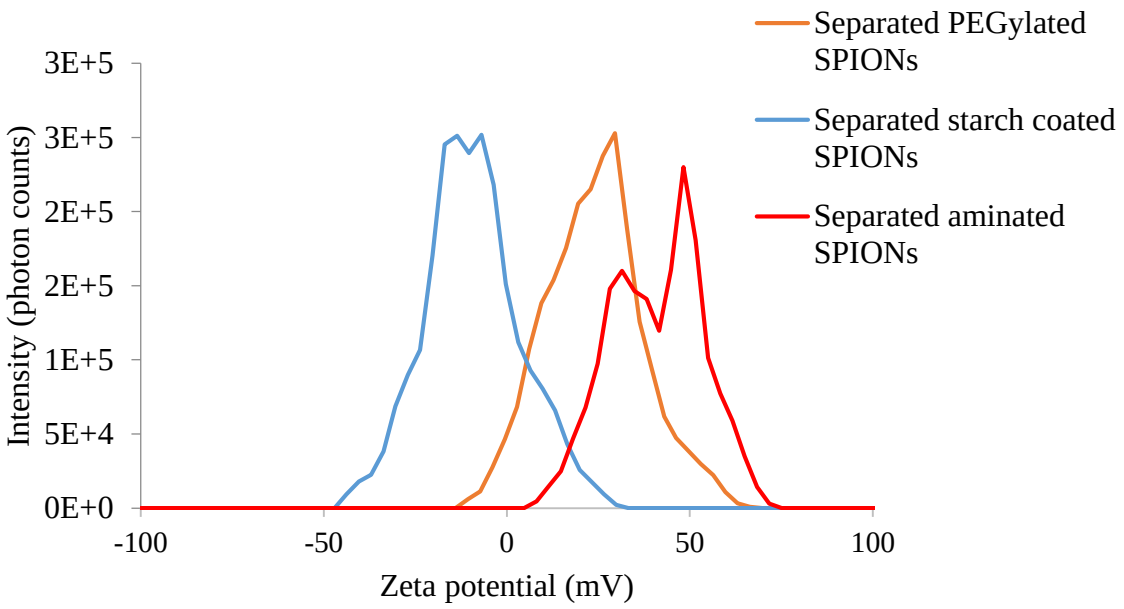

Figure 45. Zeta potential measurement of the surface separated PEGylated, starch coated and animated SPIONs.

2.13: Future Work – Improvement of composition homogeneity of SPIONs

2.13.1: Introduction

SPIONs were usually synthesized with a shell and core structure. The shell is usually made of long chain polymers and the core is usually 70-90 % magnetite which leave 10-90% of other crystal structure or other materials. The content of the magnetite has a direct impact on its magnetic properties, which is extremely important for MRI related studies. Beside particle size distribution, which directly affect the amount of magnetite content, the composition of the SPION core is the major factor for inconsistent MRI enhancement. Different synthesis methods will produce SPIONs with different magnetite purity distribution. Currently, there is no method to separate SPIONs with composition difference. Therefore, we are suggesting a methodology to purify the core composition of SPIONs.

2.13.2: Experiment

During the size separating of our previous work, some MF-SPIONs showed a similar average size under different magnetic field as shown in **Figure 46**. Further investigation was done to confirm their magnetic susceptibility. Three samples were MF separated into a similar average particle size under three different external magnetic fields. Magnetic susceptibilities were measured for all of three MF-SPIONs and showed very different magnetic properties as shown in **Figure 47**.

2.13.3: Results

The preliminary result showed that particular magnetic composition could be selected out by the size separation method, which needs to be confirmed with the DMF. The DMF method with narrow and controlled size distribution should provide an explanation whether the

preliminary results were affected by the size distribution of the three MF-SPIONs. However, the experiment is currently still in progress, and more work needs to be done to confirm whether the result was indeed caused by different magnetic composition. A combination the DMF and X-Ray diffraction technique will be used to provide the relationship with different crystal structures of the SPIONs.

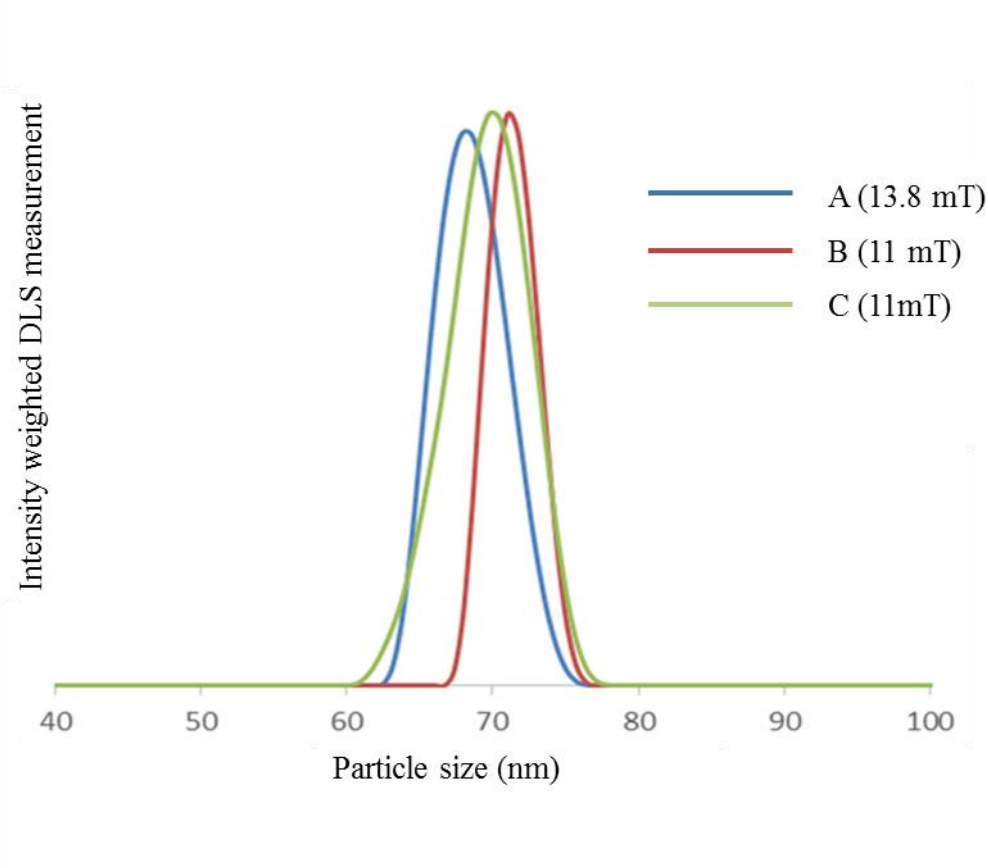

Figure 46. DLS measurement of three MF-SPIONs, which separated in three different magnetic fields. All three MF-SPIONs have almost the same average size.

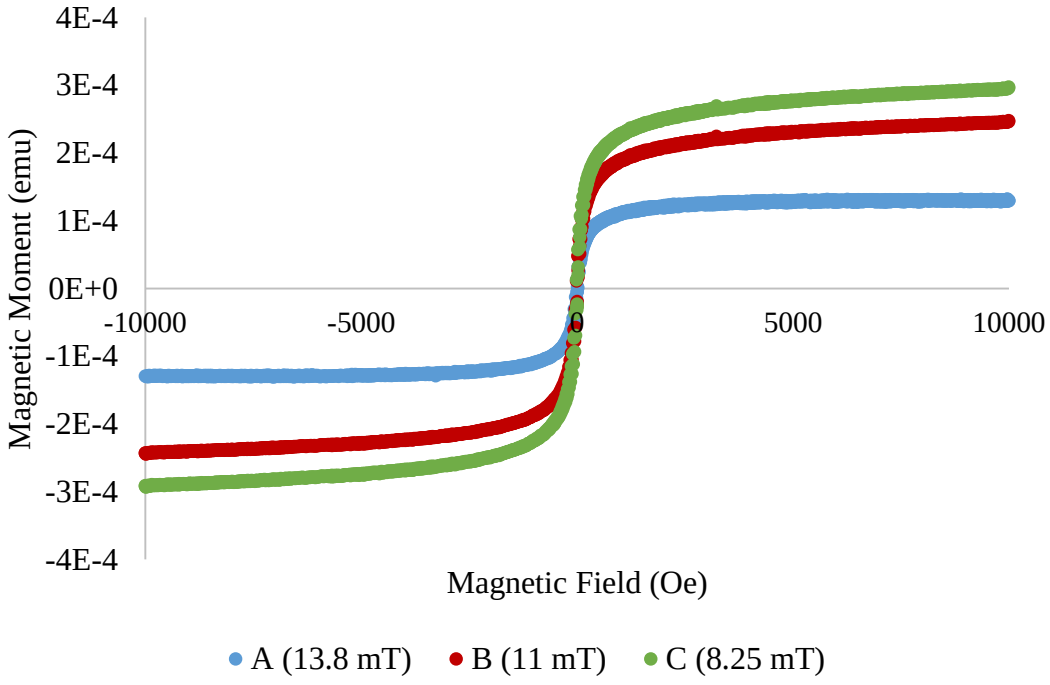

Figure 47. SQUID measurement of magnetic susceptibility of sample A, B and C which was separated in three different magnetic field during MF process.

References:

(1) Sonavane, G.; Tomoda, K.; Makino, K. *Colloids Surfaces B Biointerfaces* **2008**, *66* (2), 274–280.

(2) Huang, J.; Bu, L.; Xie, J.; Chen, K.; Cheng, Z.; Li, X.; Chen, X. *ACS Nano* **2010**, *4* (12), 7151–7160.

(3) Huang, T.; Xu, X. N.; Huang, S. T. *J. Mater. Chem.* **2010**, *20* (44), 9867–9876.

(4) Liu, F.; Hou, Y.; Gao, S. *Chem. Soc. Rev.* **2014**, *43* (23), 8098–8113.

(5) Kalvius, G.; Tebble, R. *Experimental Magnetism*; 1979.

(6) Gittleman, J. I.; Abeles, B.; Bozowski, S. *Phys. Rev. B* **1974**, *9* (9), 3891–3897.

(7) Butler, R. F. *J. Geophys. Res.* **1975**, *80* (29).

(8) Dunlop, D. J. *J. Geophys. Res.* **1974**, *79* (35), 5537.

(9) Si, S.; Kotal, A.; Mandal, T. K.; Giri, S.; Nakamura, H.; Kohara, T. **2004**, No. 11, 3489–3496.

(10) Cole, A. J.; Yang, V. C.; David, A. E. *Trends Biotechnol.* **2011**, *29* (7), 323–332.

(11) Gupta, a; Gupta, M. *Biomaterials* **2005**, *26* (18), 3995–4021.

(12) Townsend, J.; Burtovyy, R.; Galabura, Y.; Luzinov, I. *ACS Nano* **2014**, *8* (7), 6970–6978.

(13) Qi, K.; Al-Haideri, M.; Seo, T.; Carpentier, Y. A.; Deckelbaum, R. J. *J. Parenter. Enter. Nutr.* **2003**, *27* (1), 58–64.

(14) Corot, C.; Robert, P.; Idée, J. M.; Port, M. *Adv. Drug Deliv. Rev.* **2006**, *58* (14), 1471–1504.

(15) FDA. Approved Drug Products with Therapeutic Equivalence Evaluations http://www.accessdata.fda.gov/scripts/cder/ob/docs/tempai.cfm.

(16) Thiesen, B.; Jordan, A. *Int.J Hyperth.* **2008**, *24* (1464-5157 (Electronic)), 467–474.

(17) Maier-Hauff, K.; Ulrich, F.; Nestler, D.; Niehoff, H.; Wust, P.; Thiesen, B.; Orawa, H.; Budach, V.; Jordan, A. *J. Neurooncol.* **2011**, *103* (2), 317–324.

(18) Laurent, S.; Forge, D.; Port, M.; Roch, A.; Robic, C.; Vander Elst, L.; Muller, R. N. *Chem. Rev.* **2008**, *108* (6), 2064–2110.

(19) Xie, J.; Huang, J.; Li, X.; Sun, S.; Chen, X. *Curr. Med. Chem.* **2009**, *16* (10), 1278–1294.

(20) Briley-Saebo, K. C.; Mani, V.; Hyafil, F.; Cornily, J. C.; Fayad, Z. A. *Magn. Reson. Med.* **2008**, *59* (4), 721–730.

(21) Wang, Y.-X. J.; Hussain, S. M.; Krestin, G. P. *Eur. Radiol.* **2001**, *11* (11), 2319–2331.

(22) Johannsen, M.; Gneveckow, U.; Thiesen, B.; Taymoorian, K.; Cho, C. H.; Waldöfner, N.; Scholz, R.; Jordan, A.; Loening, S. A.; Wust, P. *Eur. Urol.* **2007**, *52* (6), 1653–1662.

(23) Pradal, J.; Maudens, P.; Gabay, C.; Seemayer, C. A.; Jordan, O.; Allémann, E. *Int. J. Pharm.* **2016**, *498* (1-2), 119–129.
(24) Hunter Bradley Rogers. Size Optimization of Magnetic Nanoparticles for Biomedical Applications via a Novel Size-Selective Fractionation Process, 2014.
(25) Jung, C. W.; Jacobs, P. *Magn. Reson. Imaging* **1995**, *13* (5), 661–674.
(26) Li, Y.; Chen, T.; Tan, W.; Talham, D. R. *Langmuir* **2014**, *30* (20), 5873–5879.
(27) Eric D. Smolensky, Hee-Yun E. Park, Yue Zhou, Gabriele A. Rolla, M.; Marjańska, Mauro Botta, and V. C. P. *J Mater Chem B Mater Biol Med* **2013**, *1* (22), 2818–2828.
(28) Lartigue, L.; Hugounenq, P.; Alloyeau, D.; Clarke, S. P.; Lévy, M.; Bacri, J.-C.; Bazzi, R.; Brougham, D. F.; Wilhelm, C.; Gazeau, F. *ACS Nano* **2012**, *6* (12), 10935–10949.
(29) Absar Ahmad, *,†; Satyajyoti Senapati, ‡; M. Islam Khan, †; Rajiv Kumar, ‡ and; Murali Sastry*, §. **2003**.
(30) Stöber, W.; Fink, A.; Bohn, E. *J. Colloid Interface Sci.* **1968**, *26* (1), 62–69.
(31) Matsumura, Y.; Maeda, H. *Cancer Res.* **1986**, *46* (12), 6387–6392.
(32) Park, K. *ACS Nano* **2013**, *7* (9), 7442–7447.
(33) Owens, D. E.; Peppas, N. A. *Int. J. Pharm.* **2006**, *307* (1), 93–102.
(34) Li, S. D.; Huang, L. *Mol. Pharm.* **2008**, *5* (4), 496–504.
(35) Sonaje, K.; Lin, K. J.; Wey, S. P.; Lin, C. K.; Yeh, T. H.; Nguyen, H. N.; Hsu, C. W.; Yen, T. C.; Juang, J. H.; Sung, H. W. *Biomaterials* **2010**, *31* (26), 6849–6858.
(36) Albanese, A.; Tang, P. S.; Chan, W. C. W. *Annu. Rev. Biomed. Eng.* **2012**, *14* (1), 1–16.
(37) Arami, H.; Khandhar, A.; Liggitt, D.; Krishnan, K. M. *Chem. Soc. Rev.* **2015**, *42* (12), 4906.
(38) Zong, Y.; Guo, J.; Ke, T.; Mohs, A. M.; Parker, D. L.; Lu, Z. R. *J. Control. Release* **2006**, *112* (3), 350–356.
(39) Jinno, J. I.; Kamada, N.; Miyake, M.; Yamada, K.; Mukai, T.; Odomi, M.; Toguchi, H.; Liversidge, G. G.; Higaki, K.; Kimura, T. *J. Control. Release* **2006**, *111* (1-2), 56–64.
(40) Yadav, K. S.; Chuttani, K.; Mishra, A. K.; Sawant, K. K. *PDA J. Pharm. Sci. Technol.* **2011**, *65* (2), 131–139.
(41) Weissleder, R.; Elizondo, G.; Wittenberg, J.; Rabito, C. a; Bengele, H. H.; Josephson, L. *Radiology* **1990**, *175* (2), 489–493.
(42) Kulkarni, S. A.; Feng, S.-S. *Pharm. Res.* **2013**, *30* (10), 2512–2522.
(43) Duplessis, J.; Ramachandran, C.; Weiner, N.; Muller, D. *Int. J. Pharm.* **1994**, *103* (3), 277–282.
(44) Chono, S.; Tanino, T.; Seki, T.; Morimoto, K. *J. Drug Target.* **2008**.
(45) Shellock, F. G.; Kanal, E. *J. Magn. Reson. Imaging* **1999**, *10* (3), 477–484.
(46) Grobner, T.; Prischl, F. C. *Kidney Int.* **2007**, *72* (3), 260–264.

(47) Faucher, L.; Tremblay, M.; Lagueux, J.; Gossuin, Y.; Fortin, M. A. *ACS Appl. Mater. Interfaces* **2012**, *4* (9), 4506–4515.
(48) Jordan, A.; Wust, P.; Fähling, H.; John, W.; Hinz, A.; Felix, R. *Int. J. Hyperthermia 9* (1), 51–68.
(49) Di Corato, R.; Espinosa, A.; Lartigue, L.; Tharaud, M.; Chat, S.; Pellegrino, T.; Ménager, C.; Gazeau, F.; Wilhelm, C. *Biomaterials* **2014**, *35* (24), 6400–6411.
(50) Stauffer, P. R.; Cetas, T. C.; Jones, R. C. *IEEE Trans. Biomed. Eng.* **1984**, *BME-31* (2), 235–251.
(51) Dozier, D.; Palchoudhury, S.; Bao, Y. *J. Sci. Heal. …* **2010**, 16–18.
(52) Gutiérrez, L.; Costo, R.; Grüttner, C.; Westphal, F.; Gehrke, N.; Heinke, D.; Fornara, A.; Pankhurst, Q. A.; Johansson, C.; Veintemillas-Verdaguer, S.; Morales, M. P.; Colombo, M.; Carregal-Romero, S.; Casula, M. F. *Dalt. Trans.* **2015**, *44* (7), 2943–2952.
(53) Gordon, R. T.; Hines, J. R.; Gordon, D. *Med. Hypotheses* **1979**, *5* (1), 83–102.
(54) Gaumet, M.; Vargas, A.; Gurny, R.; Delie, F. *Eur. J. Pharm. Biopharm.* **2008**, *69* (1), 1–9.
(55) Dudeck, O.; Bogusiewicz, K.; Pinkernelle, J.; Gaffke, G.; Pech, M.; Wieners, G.; Bruhn, H.; Jordan, A.; Ricke, J. *Invest Radiol* **2006**, *41* (6), 527–535.
(56) Kumar, C. S. S. R.; Mohammad, F. *Adv. Drug Deliv. Rev.* **2011**, *63* (9), 789–808.
(57) Hilger, I.; Hiergeist, R.; Hergt, R.; Winnefeld, K.; Schubert, H.; Kaiser, W. A. *Invest. Radiol.* **2002**, *37* (10), 580–586.
(58) Tanaka, K.; Ito, A.; Kobayashi, T.; Kawamura, T.; Shimada, S.; Matsumoto, K.; Saida, T.; Honda, H. *J. Biosci. Bioeng.* **2005**, *100* (1), 112–115.
(59) Hergt, R.; Dutz, S.; Michael, R.; Röder, M. *J. Phys. Condens. Matter* **2008**, *20* (38), 385214.
(60) Hergt, R.; Dutz, S.; Müller, R.; Zeisberger, M. *J. Phys. Condens. Matter* **2006**, *18* (38), S2919–S2934.
(61) Sheng, Peng; Shouheng, S. *Mater. Matters* **2009**, *4* (1), 14.
(62) Jordan, A.; Scholz, R.; Wust, P.; Schirra, H.; Schmidt, H.; Felix, R. *J. Magn. Magn. Mater.* **1999**, *194* (1-3), 185–196.
(63) Jordan, A.; Scholz, R.; Wust, P.; Fähling, H.; Roland Felix. *J. Magn. Magn. Mater.* **1999**, *201* (1-3), 413–419.
(64) Soheilian, R.; Choi, Y. S.; David, A. E.; Abdi, H.; Maloney, C. E.; Erb, R. M. *Langmuir* **2015**, *31* (30), 8267–8274.
(65) Min, K. A.; Shin, M. C.; Yu, F.; Yang, M.; David, A. E.; Yang, V. C.; Rosania, G. R. *ACS Nano* **2013**, *7* (3), 2161–2171.
(66) Wust, P. D. P.; Gneveckow, U.; Johannsen, M.; Böhmer, D.; Henkel, T.; Kahmann, F.; Sehouli, J.; Felix, R.; Ricke, J.; Jordan, A.

http://dx.doi.org/10.1080/02656730601106037 **2009**.

(67) Harrison, R. J.; Dunin-Borkowski, R. E.; Putnis, A. *Proc. Natl. Acad. Sci. U. S. A.* **2002**, *99* (26), 16556–16561.

(68) Tromsdorf, U. I.; Bruns, O. T.; Salmen, S. C.; Beisiegel, U.; Weller, H. *Nano Lett.* **2009**, *9* (12), 4434–4440.

(69) Amstad, E.; Gillich, T.; Bilecka, I.; Textor, M.; Reimhult, E. *Nano Lett.* **2009**, *9* (5), 4042–4048.

(70) Amstad, E.; Zurcher, S.; Mashaghi, A.; Wong, J. Y.; Textor, M.; Reimhult, E. *Small* **2009**, *5* (11), 1334–1342.

(71) Park, J.; Lee, E.; Hwang, N. M.; Kang, M.; Sung, C. K.; Hwang, Y.; Park, J. G.; Noh, H. J.; Kim, J. Y.; Park, J. H.; Hyeon, T. *Angew. Chemie - Int. Ed.* **2005**, *44* (May), 2872–2877.

(72) Liang, X.; Wang, X.; Zhuang, J.; Chen, Y.; Wang, D.; Li, Y. *Adv. Funct. Mater.* **2006**, *16* (14), 1805–1813.

(73) Yu, W. W.; Falkner, J. C.; Yavuz, C. T.; Colvin, V. L. *Chem. Commun. (Camb).* **2004**, No. 20, 2306–2307.

(74) Zhu, Y.; Jiang, F. Y.; Chen, K.; Kang, F.; Tang, Z. K. *J. Alloys Compd.* **2011**, *509* (34), 8549–8553.

(75) Cavelius, C.; Moh, K.; Mathur, S. *Cryst. Growth Des.* **2012**, *12* (12), 5948–5955.

(76) Park, J.; An, K.; Hwang, Y.; Park, J.-G.; Noh, H.-J.; Kim, J.-Y.; Park, J.-H.; Hwang, N.-M.; Hyeon, T. *Nat. Mater.* **2004**, *3* (12), 891–895.

(77) Jarrett, B. R.; Frendo, M.; Vogan, J.; Louie, A. Y. *Nanotechnology* **2007**, *18* (3), 35603.

(78) Gutiérrez, L.; Costo, R.; Grüttner, C.; Westphal, F.; Gehrke, N.; Heinke, D.; Fornara, A.; Pankhurst, Q. a; Johansson, C.; Morales, M. P. *Dalt. Trans.* **2015**, No. December, 2943–2952.

(79) Stolnik, S.; Illum, L.; Davis, S. S. *Adv. Drug Deliv. Rev.* **2012**, *64* (SUPPL.), 290–301.

(80) Gurav, A.; Kodas, T.; Pluym, T.; Xiong, Y. *Aerosol Sci. Technol.* **1993**, *19* (4), 411–452.

(81) Lee, C. S.; Lee, H.; Westervelt, R. M. *Appl. Phys. Lett.* **2001**, *79* (20), 3308.

(82) Rishton, S. a.; Lu, Y.; Altman, R. a.; Marley, a. C.; Bian, X. P.; Jahnes, C.; Viswanathan, R.; Xiao, G.; Gallagher, W. J.; Parkin, S. S. P. *Microelectron. Eng.* **1997**, *35* (December 2015), 249–252.

(83) Hyeon, T. *Chem. Commun.* **2003**, *8* (8), 927–934.

(84) Tocher, D. A. *Appl. Organomet. Chem.* **2000**, *14* (3), 172–173.

(85) Bagwe, R. P.; Kanicky, J. R.; Palla, B. J.; Patanjali, P. K.; Shah, D. O. *Crit. Rev. Ther. Drug Carrier Syst.* **2001**, *18* (1), 77–140.

(86) Gupta, A. K.; Curtis, A. S. G. *Biomaterials* **2004**, *25* (15), 3029–3040.

(87) Kim, D. K.; Zhang, Y.; Voit, W.; Rao, K. V.; Muhammed, M. *J. Magn. Magn. Mater.* **2001**, *225* (1-2), 30–36.
(88) Boistelle, R.; Astier, J. P. *J. Cryst. Growth* **1988**, *90* (1-3), 14–30.
(89) Banfield, J. F.; Welch, S. a; Zhang, H.; Ebert, T. T.; Penn, R. L. *Science* **2000**, *289* (5480), 751–754.
(90) Penn, R. L.; Banfield, J. F. *Geochim. Cosmochim. Acta* **1999**, *63* (10), 1549–1557.
(91) Penn, R. L.; Banfield, J. F. *Science (80-.).* **1998**, *281* (5379), 969–971.
(92) Binh, V. T.; Purcell, S. T.; Semet, V.; Feschet, F. *Appl. Surf. Sci.* **1998**, *130-132*, 803–814.
(93) Taylor, a. P.; Barry, J. C.; Webb, R. I. *J. Microsc.* **2001**, *201* (January), 84–106.
(94) Fendler, J. H. *Chem. Rev.* **1987**, *87* (5), 877–899.
(95) Sugimoto, T. *Adv. Colloid Interface Sci.* **1987**, *28*, 65–108.
(96) Luisi, P.; Straub, B. **1983**.
(97) Dahneke, B. E. *Measurement of suspended particles by quasi-elastic light scattering*; New York, 1983; Vol. 21.
(98) Rheinlander, T.; Kotitz, R.; Weitschies, W.; Semmler, W. *J. Magn. Magn. Mater.* **2000**, *219* (2), 219–228.
(99) Liu, C.; Wu, X.; Klemmer, T.; Shukla, N.; Yang, X.; Weller, D.; Roy, A. G.; Tanase, M.; Laughlin, D. *J. Phys. Chem. B* **2004**, *108* (20), 6121–6123.
(100) Xie, J.; Peng, S.; Brower, N.; Pourmand, N.; Wang, S. X.; Sun, S. *Pure Appl. Chem.* **2006**, *78* (5), 1003–1014.
(101) Zhao, F.; Yuan, M.; Zhang, W.; Gao, S. *J. Am. Chem. Soc.* **2006**, *128* (36), 11758–11759.
(102) Kang, J.; Lee, H.; Kim, Y.-N.; Yeom, A.; Jeong, H.; Lim, Y. T.; Hong, K. S. *Nanoscale Res. Lett.* **2013**, *8* (1), 376.
(103) Rheinländer, T.; Kötitz, R.; Weitschies, W.; Semmler, W. *Colloid Polym. Sci.* **2000**, *278* (3), 259–263.
(104) Hasegawa, K.; Sato, T. *J. Appl. Phys.* **1967**, *38* (12), 4707–4713.
(105) Constantinides, C. D.; Rogers, J.; Herzka, D. A.; Boada, F. E.; Bolar, D.; Kraitchman, D.; Gillen, J.; Bottomley, P. A. *Magn. Reson. Med.* **2001**, *46* (6), 1164–1168.
(106) Allkemper, T.; Bremer, C.; Matuszewski, L.; Ebert, W.; Reimer, P. *Radiology* **2002**, *223* (2), 432–438.
(107) Chastellain, M.; Petri, A.; Hofmann, H. *J. Colloid Interface Sci.* **2004**, *278* (2), 353–360.
(108) Chambon, C.; Clement, O.; Le Blanche, A.; Schouman-Claeys, E.; Frija, G. *Magn. Reson. Imaging* **1992**, *11* (4), 509–519.
(109) Yoshida, T.; Othman, N. B.; Enpuku, K. *J. Appl. Phys.* **2013**, *114* (17), 173908.
(110) Glöckl, G.; Brinkmeier, V.; Aurich, K.; Romanus, E.; Weber, P.; Weitschies, W. *J.*

Magn. Magn. Mater. **2005**, *289*, 480–483.
(111) Malvern Instruments. *Dynamic Light Scattering*; 2011.
(112) Cole, A. J.; David, A. E.; Wang, J.; Galbán, C. J.; Hill, H. L.; Yang, V. C. **2012**, *32* (8), 2183–2193.
(113) Griffiths, D. J. *An Introduction to Electrodynamics*; 2007; Vol. 110.